Estimation of the Bed Shear Stress in Vegetated and Bare Channels

by

Qingjun (Judy) Yang

B.S., Zhejiang University (2013)

Submitted to the Department of Civil and Environmental Engineering
in partial fulfillment of the requirements for the degree of

Master of Science in Civil and Environmental Engineering

at the

MASSACHUSETTS INSTITUTE OF TECHNOLOGY

June 2015

Signature redacted

Author .....
Department of Civil and Environmental Engineering
May 8, 2015

Signature redacted

Certified by .....
Heidi M. Nepf
Donald and Martha Harleman Professor of Civil and Environmental Engineering
Thesis Supervisor

Signature redacted

Accepted by .....
Heidi M. Nepf
Chair, Departmental Committee for Graduate Students

Estimation of the Bed Shear Stress in Vegetated and Bare Channels

by

Qingjun (Judy) Yang

Submitted to the Department of Civil and Environmental Engineering
on May 8, 2015, in partial fulfillment of the
requirements for the degree of
Master of Science in Civil and Environmental Engineering

Abstract

The shear stress at the bed of a channel influences important benthic processes such as sediment transport. Several methods exist to estimate the bed shear stress in bare channels without vegetation, but most of these are not appropriate for vegetated channels due to the impact of vegetation on the velocity profile and turbulence production. This study proposes a new model to estimate the bed shear stress in both vegetated and bare channels with smooth beds. The model, which is supported by measurements, indicates that for both bare and vegetated channels with smooth beds, within a viscous sub-layer at the bed, the viscous stress decreases linearly with increasing distance from the bed, resulting in a parabolic velocity profile at the bed. For bare channels, the model describes the velocity profile in the overlap region of the Law of the Wall. For emergent canopies of sufficient density (frontal area per unit canopy volume $a \geq 4.3m^{-1}$), the thickness of the linear-stress layer is set by the stem diameter, leading to a simple estimate for bed shear stress.

Thesis Supervisor: Heidi M. Nepf
Title: Donald and Martha Harleman Professor of Civil and Environmental Engineering

Acknowledgments

Foremost, I would like to express my deepest gratitude to my adviser, Professor Heidi M. Nepf, who guide me in my research with great patience and passion. I would not have so much progress in the past two years without her instruction and encouragement. She helps me whenever I have trouble understanding something, either it is an equation, a concept or an American joke. I am thankful for all her encouragement, which helps me becoming a mature researcher. I also tremendously appreciate the freedom and support she gave me to pursue my interests.

Second, I would like to thank Francois Kerger for contributing data and ideas for this study. His work guided me into the research of vegetation hydrodynamics.

Third, I would like to thank my labmates who helped me adapting to the new environment, especially Jeff Rominger, Elizabeth Follett, Alejandra Ortiz, John Kindziolka, Erin Connor and Julia Hopkins. I also thank my friends at Parson's lab, Pierce Lab and other departments, especially Jen Nguyen, Ruby Fu, Jiawei Zhou for being supportive to me all the time. I thank my family and friends at China and all over the world for caring about me.

Finally, The work was supported by NSF Grant EAR 1414499. The data for the color map in Fig.5-1 is provided by Guillermo Palau Salvador, Thorsten Stoesser, Andreas Christof Rummel, and Wolfgang Rodi. I thank Francesco Ballio and two other anonymous reviewers for their useful comments.

Contents

List of Figures

List of Tables

Chapter 1

Introduction

1.1 Ecosystem services of aquatic and riparian vegetation

Aquatic and riparian vegetation are, respectively, the vegetation living in fresh- and salt water and those living in the interface between water and land. In addition to contributing to the global food yield [14], aquatic and riparian vegetation play an important role in the functioning of our ecological systems, such as stabilizing banks, beds and shorelines, purifying water, providing habitat for invertebrates and other organisms, and attenuating waves and storms [59, 5, 61]. Conservative economical evaluation shows that seagrass contributes 3.8 trillion dollars per year to our global ecosystem by cycling nutrients, and wetlands contribute around 1.4 trillion dollars per year by treating waste water [18]. Most of this value is currently outside the market.

Recently, increasing attention has turned to the study of the ecosystem services of aquatic and riparian vegetation due to the deterioration of our ecological environment. In 1998, nearly 40% of the assessed river miles in the U.S. was found to suffer from excessive sediment [3]. According to EPA's recent survey in 2008 and 2009, 55% of the U.S. river and stream length is in poor biological condition and 40% of it has high levels of phosphorus and 28% has high levels of nitrogen[4]. According to the Chinese

SEPA report in 2014, 17 out of 31 major lakes in China are polluted, and 28.3% of the main rivers are non-drinkable [69]. It is estimated that each year 190 million Chinese get sick and 60,000 die because of water pollution [78]. Vegetation, with its unique ability to remedy water pollution, has became a common tool in the restoration of rivers, streams, and wetlands [59, 7, 5]. This section is focused on discussing the different roles the aquatic and riparian vegetation plays in ecosystem services.

1.1.1 Vegetation and erosion

Aquatic and riparian vegetation are recognized for their ability to reduce erosion in channels [89, 1, 2] and coastal areas[108, 30, 71]. Field observation in streambanks shows that vegetation is able to reduce erosion and stabilize banks [89, 6, 58]. In southern British Columbia, researchers found that major bank erosion happened 30 times more frequently on non-vegetated stream bends than on vegetated bends [6]. Streams with vegetation were also found to retained up to 80% of the sediment in transit downstream [84], and, similarly, a vegetated reach retained 50% more corn pollen than an unvegetated reach of similar length [106]. The observations in the field have been confirmed in laboratory studies. In particular, Steven Abt and colleagues constructed a meandering stream channel in a recirculating flume based on the configuration of natural streams [2]. By injecting sediment into the simulated stream at different release rate through a filled sediment hopper, they compared the amount of sediment deposition with and without vegetation in the stream. The amount of sediment retained after flushing sediment-free water was also compared for bare and vegetated streams. The study showed that the presence of vegetation significantly increases the amount of sediment deposition and retention.

In coastal areas, vegetation also plays an important role in preventing erosion [108, 30, 71]. By comparing the photographs taken before and after the disappearance of the seagrass, Zostera Marina, Douglas Wilson [108] found that the level of the seabed was lowered by 2ft after the die out of the seagrass and the bed became more stony due to the erosion of fine sediments. Replanted mangroves were also proven to be a successful way to protect coastal areas from erosion [71]. In particular, bunds

(the constructed earth dykes) behind the mangroves were protected from erosion, and as a result the agriculture areas behind the bunds were saved from erosion.

The reduction of erosion by vegetation has been attributed to the reduction of flow velocity in the vegetated area [24, 84, 80]. In general, low velocity reduces erosion and promotes sedimentation [84, 49, 80]. The existence of vegetation introduces additional drag to the flow [63], which dissipates energy and slows down the flow, and as such reduces erosion and promotes deposition. Field observation shows that submerged vegetation can reduce velocity up to ten fold compared to adjacent non-vegetated regions[88]. The flow reduction is more significant for emergent vegetation, because emergent vegetation produces more drag than submerged vegetation. Two recent studies partitioned sediment deposition inside a vegetated channel into two parts: the primary deposition, which accounts for the deposition of sediment that hasn't been deposited before, such as the sediments from run off, and the suspended flux of sediments that were deposited and resuspended from within the vegetated region [30, 73]. Because the chemical compounds in the already deposited bottom sediments might be different from the newly arrived suspended sediments, such partition can help us understand the nutrient and chemical exchange between bottom sediments and open water [73]. By assuming that the suspended flux declines exponentially with increasing distance above the bed, Gacia and Duarte found that seagrass reduces bed erosion mainly by preventing the resuspension of bed sediments[30].

In addition to the flow reduction caused by vegetation, researchers also found that the surface of the vegetation acts like a distributed sediment sink [24, 48]. Specifically, for vegetation that is not a perfect vertical cylinder, there is distributed horizontal surface in the water column. The horizontal surface acts like a sediment sink because sediment that deposited on the horizontal surface tends to slide down and accumulate in the bed. In the presence of vines at flow velocity $\approx 10mm/s$, the total amount of sediment deposition attributed to plant surface roughly equals the sediment deposition directly into the bed.

While it has been widely accepted that the fluid mechanics above the bed has a large impact on the erosion and deposition in a vegetated channel, many researchers

seek to understand the impact of vegetation roots on erosion [90, 34, 35]. Studies show that the tensile stress provided by fibrous roots increases the soil cohesion and reduces erosion [90, 75]. For overland flow, however, researchers have found that the above-ground biomass plays a more important role in controlling erosion [76]. By progressively clipping the grass cover, Prosser et. al. found that the above-ground biomass decreases the erosion by two orders of magnitude compared to the roots-only grass [76]. The fluid mechanics associated with the above-ground biomass is the focus of this thesis.

1.1.2 Vegetation and water quality

Rapid growth of industry and urbanization promote the release of waste water that contains nitrate, phosphorus, organic compound and heavy metal [91, 101]. Excessive nitrogen and phosphorus has been identified as a major cause of algae blooms that reduce dissolved oxygen, suffocate aquatic life, and produce toxins that are harmful to human beings [77]. In 2007, excess phosphorus and nitrogen caused a gigantic bloom of cyanobacteria in Taihu lake, which provided drinking water for over 2-million people, and supported one of China's most important fisheries for fishes and crab [33]. The toxins produced by some cyanobacteria can cause damage to the liver, intestines and nervous systems [33]. The nitrate in drinking water also causes infant methemoglobinemia [44]. High nitrate concentration in 19.8% of the water samples collected in the Great Lakes was found to cause lethal and sublethal effects in amphibians [81]. Excessive organic compounds in the water can also cause oxygen depletion and severe damage to aquatic life. Heavy metal, even at small amounts, creates risk to human health as well[41]. To combat these pollutants, vegetation has been widely used in waste water treatment. This is because vegetation can significantly improve water quality by filtering excess nitrogen, phosphorus, carbon and dissolved metals[36, 54, 59].

Experiments in controlled wetlands and rivers with and without vegetation show that vegetation significantly increases the amount of N and P removed from the water [100, 88]. By compiling previous field data, Valiela and Cole found that the vege-

tation in coastal wetlands plays an important role in filtering land-derived nitrogen, protecting seagrass from harmful levels of nutrient [104]. Seagrass is very sensitive to eutrophication, and the amount of seagrass cover lost is positively correlated to the nitrogen load in the water. By providing denitrification, which converts nitrate to nitrogen gas, and burial of land-derived N, vegetation in wetlands helps to reduce seagrass loss[104].

Vegetation increases the removal of N, P and C in the water by promoting the deposition of fine sediment [86, 88], uptaking and storing nutrient in their tissues[100], and enhancing the microbial nutrient removal by modifying environmental conditions [37, 100]. Field experiments in rivers using sediment traps and sediment cores have shown that macrophytes cause a considerable nutrient retention by slowing down flow, which increases the water residence time and the amount of deposition of fine sediment[88]. In particular, the bed sediment within and downstream of a vegetation patch contains much more fine sediment (up to 16 folds) than nonvegetated places[88]. The fine sediment has been found to contain much more organic matter, carbon, nitrogen and phosphorus than coarse sand [84]. Plants also uptake excess nutrients and store them in different parts of their body [54]. This mechanism has been used in waste water treatment [54]. By injecting ^{15}N-labeled phytodetritus into the sediment of seagrass, the uptake of nitrate through roots and the transport of nitrate to leaves have been observed [25]. Biological inspection of seagrass leaves using microscopes shows that certain seagrass leaves have no cell walls ingrowth but porous cubicles that are presumed to facilitate nutrient absorption [47, 23]. For aquatic macrophytes that live in rivers, roots have been found to play a more important role in absorbing nutrient than leaves [16]. This conclusion is based on the strong dependence of plant biomass and density on the nutrient concentration in the sediment rather than the open water [16]. Field observation of river macrophytes shows that the accumulation of organic material in vegetated channels exceeds the maximum macrophytes biomass by ten fold [86]. This suggests that sedimentation in rivers play a major role in removing nutrients from the water column. The modification of the microbial environment by vegetation also contributes to the nutrient removal. By comparing

the amount of N and P removed by wetland vegetation and the amount of N and P being absorbed in the plant tissues and standing litter, Tanner et al. found that the plant nutrient absorption, which accounts for only a small fraction of the total nutrient removal by wetlands, is not the major mechanism for the removal of nutrient by vegetation[100]. Instead, they suggest that the vegetation enhances the removal of N and P by transporting oxygen via plant shoot to root, which enhances the microbial decomposition and nitrification rates.

Aquatic and riparian vegetation acts as the largest biological sink for heavy metals and other contaminants [72, 109, 13]. Studies using trace elements show that the amount of toxic metals such as Cd, Pb, and Hg in the vegetation can be at least one order of magnitude greater than surrounding water and sediments [72]. The accumulation of heavy metals mainly in the rhizomes and roots of macrophytes suggests that macrophytes take up heavy metal mainly though their roots [87]. The increased deposition of fine sediment inside vegetation also contributes to the reduction of heavy metal in the water [96]. Fine sediments have been found to absorb heavy metal at a greater rate than larger particles, because their surfaces are usually negatively charged, such as the surfaces of clay minerals and organic matter [96]. Chemical examination of sediments of different sizes shows that most of the heavy metal are stored in fine clay and silt with size $< 63\mu m$ [105, 94, 112].

1.1.3 Vegetation and habitat

Aquatic and riparian vegetation are acknowledged for their ability to provide habitats for aquatic animals and microorganisms [38, 32]. In one study, the seasonal variation of aquatic animals in a stream was similar to the seasonal variation of plants [38], and a decrease in the overall abundance of fish was related to the increasing length of nonforested riparian reach [42]. Insects have been found to feed on aquatic vegetation [57], and epiphytes such as algae always coat macrophytes [14].

Two mechanisms contribute to the creation of habitat by vegetation: the alteration of the flow field [19] and the promotion of sediment deposition[8]. The spatial heterogeneity of flow inside a vegetation patch allows aquatic animals like fish to rest

in the low-velocity wake region and dart into the fast water for food [19, 39]. By promoting the deposition of sediments, vegetation also indirectly affects the habitats of aquatic life [8]. As summarized in [8], suspended and bed sediments have three major effects on fish: (1) suffocation through direct contact, (2) the attenuation of light by suspended sediments, which affect their feeding ability (3) burial of eggs and larva by excess sediment.

1.1.4 Other ecosystem services

In addition to the above functions, vegetation also plays an important role in protecting coastal areas from waves, extreme events like tsunami, shaping land topography and absorbing carbon [71, 20, 97, 60]. The additional flow resistance provided by vegetation dissipates wave energy, which protects the coast from tidal and wind waves, and extreme events like tsunamis [71, 55, 20]. The peak tidal wave velocity in swamps ($< 0.1m/s$) has been found to be one order of magnitude smaller than the peak tidal velocity in other regions [55]. The decay of the energy and amplitude of wind-induced surface waves in a mangrove forest has been studied theoretically [55], and the decay of random-wave height inside a vegetation field with mixed vegetation length has been studied numerically and experimentally [10]. Flume experiments using simulated emergent vegetation on a sand beach show that vegetation can significantly protect the beach from regular and irregular waves [103]. During the 2004 Indian Ocean tsunami, coastal areas with mangroves were found to suffer little damage while areas without mangroves were completely destroyed [20]. Using vegetation to protect coastal areas from tsunami has been proposed [98].

The geomorphological impact of vegetation has been extensively studied. For example, while experimental self-formed channels with only sand and water always lead to braided channels, laboratory experiments with vegetation can convert the steady-state braided channels to single channels [97]. Similarly, by placing vegetation at different places in a channel with different density, a straight channel can be transformed into a meandering channel [7]. At the same discharge, the addition of simulated riparian vegetation (dowels) can cause channel widening, which explains

why steam reaches with riparian vegetation are wider than others [56]. The flow-vegetation-sediment interaction also accounts for the erosion at the front and sides of a vegetation patch and deposition downstream and within the patch [11]. Such interaction can be used to explain the downstream growth of vegetation patches [85], and the formation of channels between patches [102].

The substantial carbon-storage in aquatic vegetated habitats has recently drawn a lot of attention [60, 74]. While the ocean stores and cycles 93% of the earth's CO_2, over 70% of all carbon storage in ocean sediments falls in vegetated habitats, which covers less than 1% of the seabed [60]. The carbon stored in the sediments of vegetated habitats can be released into the atmosphere contributing to global warming if these habitats are destroyed [74].

1.2 Sediment transport in vegetated channels

Despite the increasing effort in replanting aquatic and riparian vegetation to restore ecosystems [71, 59, 1], the amount of aquatic and riparian vegetation has been decreasing rapidly. Over the past several decades, over 110 million acres of the fresh and saltwater wetlands in the U.S. -more than half of the nation's total amount- have been lost[70]. Thousands of acres of seagrass, and miles of kelp beds vanished in the U.S.[70]. Globally, the area of the world's mangrove forests dropped by 26%, from 5.7 to 4.2 million ha[28, 20]. Between a quarter and a half of the tidal marshes in the world has died out[22]. Deforestation of riparian vegetation with an annual rate of 14.6 million ha has also been reported [12, 95]. More details about this point and the current advance in the study of sediment transport, especially in vegetated regions are discussed in the following paragraphs.

1.2.1 Impact of sediment transport in vegetated channels

Studying sediment transport processes in vegetated channels is very important for the following two reasons. First, as explained above, the ecosystem services of aquatic and riparian vegetation, such as reducing erosion and purifying water, depend on the

sediment transport processes [15]. Second, the sediment transport processes determine the existence and growth of the vegetation [17, 71, 27]. In salt marshes, the sediment fluxes are considered to be one of the key factors determining the survival of salt marshes [27]. Field observations show that wave-induced-erosion would causes the retreat of the marsh edge [21]. The sediments eroded from the edge accrete on the marsh surface helping it to keep in pace with sea level rise[21]. In the Venice lagoon, the marsh edge has retreated 1 to $2m/year$ and the marsh surface elevation increased by $1.54cm/year$[21]. Using dimensional analysis, Day et al propose that the margin retreat rate R is a linearly proportional to the wave power density [53]. Numerical simulation of salt marsh evolution due to sediment transport under different sea level scenarios has been explored[26]. The degradation of mangroves is also determined by sediment transport mechanism [71]. Specifically, the erosion of mud-flats in front of the mangroves exposes the roots of mangroves to water, and as such causes the collapse of trees and the advance of erosion into the mangrove belt [71].

Sediment transport also affects the growth of vegetation [17]. Specifically, controlled experiments with macrophytes grown in pails containing different sediments at three locations with different flow velocity show that both the flow velocity and the sediment composition affect the shoot density and biomass [17]. In particular, finer sediments favor the growth of vegetation due to the larger nutrient concentration as compared with coarser sediments [17].

1.2.2 Estimation of sediment transport

To date, sediment transport in bare channels has been extensively investigated, and multiple empirical equations have been proposed to quantify the sediment transport rate in bare channels [111, 31]. Most of these equations relate the incipient velocity of sediment transport and the sediment transport rate to the shear stress at the bed, τ_b, or the friction velocity $U_* = \sqrt{\tau_b/\rho}$, with ρ being the fluid density [9, 107]. Recent studies suggest that the sediment transport rate in vegetated channels can be related to the bed shear stress, similar to bare channel flows [43, 11, 45]. However, the typical methods used to estimate the friction velocity (U_*) in a bare channel (listed below)

are difficult or not appropriate in vegetated channels [9, 82].

First, the log-law fitting method compares the measured velocity at different heights to a logarithmic profile called the Law of the Wall [46, 65]. The friction velocity is the fitting parameter. In vegetated channels, the Law of the Wall does not apply because the velocity does not follow a logarithmic distribution near the bed for either submerged or emergent canopies [61, 50].

Second, the slope method used in bare channels is based on the balance of bed shear stress and the potential gradient due to the water surface and bed slopes, i.e. $\tau_b = \rho g s H$, in which g is the gravitational acceleration, H is the water depth, and s is the friction slope due to both surface and bed slopes. In vegetated channels, the potential forcing $\rho g s H$ balances both the bed shear stress and the stress due to the vegetative drag. Some researchers have estimated the bed shear stress by subtracting the vegetative stress from the potential forcing [43, 45]. This method is prone to large uncertainty, because both vegetative drag and the potential forcing are an order of magnitude larger than bed shear stress [43, 99].

Third, in bare channel flow, the bed shear stress can be estimated from the maximum near-bed Reynolds stress, or by extrapolating the linear profile of Reynolds stress to the bed [66]. However, the Reynolds shear stress profile inside vegetation does not increase linearly towards the bed, but rather follows a distribution dictated by the distribution of vegetation [64]. It is therefore inappropriate to apply the Reynolds stress method in vegetated channels.

Fourth, the turbulence in a bare channel is produced by the boundary shear, directly linking τ_b and the near-bed turbulent kinetic energy (TKE). Observations over a bare bed suggest $\tau_b \approx 0.2TKE$ [92]. In vegetated channels, however, the turbulence generated by the vegetation dominates the total TKE [64], so that there is no correlation between bed shear stress and turbulent kinetic energy [62].

Finally, the viscous stress at the bed provides the most rigorous estimate of the bed shear stress. However, it is the most difficult to measure, especially in the field, because it requires measurements of velocity within the viscous sub-layer, where $\tau_b = \mu \frac{du}{dz}|_{z=0}$, with μ is the dynamic viscosity of water.

From the above list, we see that the estimation of bed shear stress in a vegetated channel remains a key limitation in sediment transport studies. Rowinski [82] proposed a mixing length model to predict the bed shear stress in a channel with emergent vegetation. However, their model requires iteration and does not have a practical form. In this thesis, I propose a new model to estimate the bed shear stress in vegetated channels that has the same form in bare channels. It is important to note that our study only considers emergent vegetation, i.e. vegetation that fills the entire water column, and channels with smooth and impermeable beds. Therefore, this is only a first step toward providing a parameterization that will work for field conditions. A discussion on how this model may be extended in the future to channels with non-smooth beds can be found in the discussion section.

Chapter 2

Theory

2.1 Governing equations

To account for the spatial heterogeneity of the flow inside a canopy, time- and space-averaged (double-averaged) Navier Stokes (N-S) equations [68] are commonly employed in the study of both terrestrial canopies [29, 79] and aquatic vegetated canopies [51, 52]. We refer the interested readers to [68] for details about the double-averaging method. The double-averaged N-S equations in an emergent canopy of uniform porosity are:

$$\frac{\partial \langle \overline{u_i} \rangle}{\partial x_i} = 0 \tag{2.1}$$

$$\frac{\partial \langle \overline{u_i} \rangle}{\partial t} + \langle \overline{u_j} \rangle \frac{\partial \langle \overline{u_i} \rangle}{\partial x_j} = g_i - \frac{1}{\rho}\frac{\partial \langle \overline{p} \rangle}{\partial x_i} + \frac{1}{\rho}\frac{\partial}{\partial x_j}\left(\tau_{ij}^{disp} + \left\langle \tau_{ij}^{Rey} \right\rangle + \left\langle \tau_{ij}^{vis} \right\rangle\right) - D_i \tag{2.2}$$

Here, $u_i = (u, v, w)$ refers to the velocity along the $x_i = (x, y, z)$ axes, corresponding to the stream-wise (parallel to the bed), span-wise, and perpendicular (to the bed) directions, respectively. The overbar $\bar{}$ indicates a time average, and a single prime $'$ indicates deviation from the time average. The bracket $\langle\rangle$ indicates the spatial average. Each time-averaged variable β is expressed as the sum of the spatial average, $\langle\beta\rangle$, and a deviation from the spatial average β''. p is the pressure, and D_i is the time-mean stress due to both viscous and pressure drag exerted by the canopy in i direction. τ_{ij}^{disp},τ_{ij}^{Rey},τ_{ij}^{vis} are the time-averaged dispersive stress, local Reynolds stress

and local viscous stress, respectively, defined in Eq.2.3.

$$\tau_{ij}^{disp} = -\rho \langle \overline{u_i}'' \overline{u_j}'' \rangle \qquad \tau_{ij}^{Rey} = -\rho \overline{u_i' u_j'} \qquad \tau_{ij}^{vis} = \rho\nu \frac{\partial \overline{u_i}}{\partial x_j} \tag{2.3}$$

Here ν is the kinematic viscosity. For unidirectional flow in a straight channel, $\left(\langle \overline{u} \rangle \frac{\partial \langle \overline{u} \rangle}{\partial x}\right) / \left(\frac{1}{\rho} \frac{\partial \langle \overline{p} \rangle}{\partial x}\right) \approx \frac{U^2}{gH}$, with U representing the spatial-average of the time-averaged velocity. In our experiments, $\frac{U^2}{gH} < 5\%$, so that we neglect the non-uniformity term in the x-momentum equation. Assuming that the average perpendicular ($\langle \overline{w} \rangle$) and lateral ($\langle \overline{v} \rangle$) velocity are much smaller than the stream-wise velocity ($\langle \overline{u} \rangle$), and that the flow is steady ($\frac{\partial \langle \overline{u_i} \rangle}{\partial t} = 0$), the stream-wise momentum equation can be simplified to Eq.2.4.

$$0 = g s_b - \frac{1}{\rho} \frac{\partial \langle \overline{p} \rangle}{\partial x} + \frac{1}{\rho} \frac{\partial}{\partial z} \left(\tau_{ij}^{disp} + \left\langle \tau_{ij}^{Rey} \right\rangle + \left\langle \tau_{ij}^{vis} \right\rangle \right) - D_x \tag{2.4}$$

Here s_b is the bed slope. The vegetative drag D_x can be represented by a quadratic law [61]:

$$D_x = \frac{1}{2} \frac{C_D a}{(1-\phi)} \langle \overline{u} \rangle^2 \tag{2.5}$$

Here a is the frontal area per canopy unit volume, ϕ is the solid volume fraction, and C_D is the drag coefficient. For cylindrical stems, $\phi = (\pi/4)ad$. The pressure gradient can be approximated as $\frac{\partial \langle \overline{p} \rangle}{\partial x} = -\rho g (s_s - s_b)$, where s_s is the water surface slope with respect to a horizontal plane. The internal shear stresses (τ_{ij}^{disp},τ_{ij}^{Rey},τ_{ij}^{vis}) go to zero at the water surface ($z = Z_s$), so that a vertical integration of Eq. 2.4 from water surface Z_s to any position $z < Z_s$ above the bed yields,

$$\left(\tau_{ij}^{disp} + \left\langle \tau_{ij}^{Rey} \right\rangle + \left\langle \tau_{ij}^{vis} \right\rangle \right) |_z + \rho \int_z^{Z_s} \left[\frac{1}{2} \frac{C_D a}{1-\phi} \langle \overline{u} \rangle^2 \right] dz = \rho g s \left(Z_s - z \right) \tag{2.6}$$

Here $s = s_s$ is the friction slope. For small s, $Z_s \approx H$. The left-hand side of Eq. 2.6 shows the partitioning of total flow resistance into the internal shear stresses (first term) and the vegetation drag (second term). The third term (on the right-hand side of Eq.2.6) represents the driving force for the flow due to pressure and/or bed slope. A similar drag partition method is described in [79]. The no-slip condition at a smooth impermeable bed requires $\tau_{xz}^{Rey}|_{z=0} = \tau_{xz}^{disp}|_{z=0} = 0$, so that the spatially-averaged bed

shear stress is simply $\langle \tau_b \rangle = \left(\tau_{ij}^{disp} + \left\langle \tau_{ij}^{Rey} \right\rangle + \left\langle \tau_{ij}^{vis} \right\rangle \right) |_{z=0} = \langle \tau_{xz}^{vis} \rangle |_{z=0} = \left\langle \rho \nu \frac{\partial \overline{u}}{\partial z} |_{z=0} \right\rangle$. The effective friction velocity in a heterogeneous flow field is therefore defined as: $U_{*eff} = \sqrt{\langle \tau_b \rangle / \rho} = \sqrt{\langle \rho U_*^2 \rangle / \rho} = \sqrt{\langle U_*^2 \rangle}$, with τ_b and U_* defined as the local bed shear stress and local friction velocity, respectively. In a homogeneous flow field, τ_b and U_* are interchangeable with $\langle \tau_b \rangle$ and with U_{*eff} and $\langle U_* \rangle$, respectively.

2.2 Friction velocity over smooth beds

2.2.1 Bare channels

First, we consider flow over a smooth bed without vegetation. Because $a = 0$ and the spatial heterogeneity is small, the dispersive stress is negligible. As discussed in [65], Eq. 2.6 can be simplified to $\left(\tau_{xz}^{Rey} + \tau_{xz}^{vis} \right) |_z = \rho g s (H - z)$, which indicates that the total stress, the sum of the Reynolds stress and viscous stress, decreases linearly with distance from the bed (z). Note that the local quantities and spatially-averaged quantities are the same in a bare channel. As the Reynolds stress is zero at the bed, $\tau_b = \rho U_*^2 = \tau_{xz}^{vis}|_{z=0} = \rho g s H$, so that the bed shear stress can be estimated from the friction slope (s). Alternatively, U_* can be estimated by fitting the measured total stress to the theoretical linear distribution of total stress,

$$\tau_{tot}(z) = \left(\tau_{xz}^{Rey} + \tau_{xz}^{vis} \right) |_z = \rho U_*^2 (1 - z/H) \tag{2.7}$$

In this paper, the application of Eq.2.7 will be called the total stress method.

Another common way to estimate the bed shear stress over a smooth bare channel is to fit the measured velocity to the analytical velocity profile called the Law of the Wall [46, 65]:

$$\frac{\overline{u}(z)}{U_*} = \begin{cases} \frac{zU_*}{\nu} = Z_+ & Z_+ \leq 5 \\ \frac{1}{\kappa} ln \left(\frac{zU_*}{\nu} \right) + 5 & Z_+ \geq 30 \end{cases} \tag{2.8}$$

Here κ, the von Karman constant, is 0.41. This law is linear in the near-bed region ($Z_+ \leq 5$) and logarithmic above ($Z_+ \geq 30$). A buffer layer exists between these two

regions, i.e. $5 \leq Z_+ \leq 30$, for which the Law of the Wall gives no formulation.

Within a thin inner layer ($Z_+ \leq 5$), the Law of the Wall assumes that the viscous stress is constant, which is associated with a linear velocity profile (first line of Eq.2.8). In contrast to this, if we assume that the Reynolds stress is negligible close to the wall, Eq.2.7 reduces to $(\tau_{xz}^{vis})\,|_z = \rho g s(H-z)$, indicating that the viscous stress should vary linearly with z close to the bed. We define the linear-stress layer height, H_v, as the height above the bed at which the linear-stress distribution can be extrapolated to zero stress. Note that the Law of the Wall assumption of constant stress remains valid at some distance less than H_v from the wall, i.e. in the limit of $z \to 0$, the linear stress assumption and constant stress assumption are congruent.

The linear viscous stress distribution and the associated parabolic velocity profile can be expressed as:

$$\tau^{vis} = \rho\nu\frac{\partial\overline{u}}{\partial z} = \rho\frac{{U_*}^2}{H_v}(H_v - z) \qquad z \leq H_v \tag{2.9}$$

$$\overline{u}\,(z) = \frac{{U_*}^2}{\nu}\left(z - \frac{z^2}{2H_v}\right) \qquad z \leq H_v \tag{2.10}$$

Note that because the flow is homogeneous in a bare channel, the locally-defined equations (Eq.2.7, 2.8, 2.9 and 2.10) are also valid for spatially-averaged value, i.e. also apply if $\overline{u}$ and U_* are replaced by $\langle\overline{u}\rangle$ and $\langle U_*\rangle$.

2.2.2 Channels with emergent vegetation

Now, let us consider the situation with vegetation on a smooth bed. However, we specifically consider regions of the flow for which the distance to the bed is smaller than the distance to the nearest stem, such that the viscous stress and the velocity are controlled by the proximity to the bed in a manner similar to that described above for the bare channel. Namely, the near-bed viscous stress should also follow the linear-stress model. We anticipate that this description will fail at some distance close to a cylinder, at which the cylinder surface also contributes to local viscous stress. In addition, we specifically note that this description will not hold within one

diameter of each cylinder (stem), because of secondary flow structures that exist in this region (e.g. [93]). In a model canopy of emergent vegetation (array of circular cylinders), previous studies [63, 67, 50] have shown that the stream-wise velocity in the upper water column (i.e. away from the bed) is vertically uniform, such that $\tau^{vis} = \rho\nu\frac{\partial\overline{u}}{\partial z} = 0$ in the upper layer of the model emergent canopy. We therefore propose the following model for the distribution of viscous stress in regions at least one diameter away from the stems inside an emergent canopy:

$$\tau^{vis} = \begin{cases} \rho\frac{{U_*}^2}{H_v}(H_v - z) & z < H_v \\ 0 & z \geq H_v \end{cases} \tag{2.11}$$

The following velocity distribution is consistent with 2.11 and a no-slip condition at the bed:

$$\overline{u}(z) = \begin{cases} \frac{{U_*}^2}{\nu}\left(z - \frac{z^2}{2H_v}\right) & z \leq H_v \\ \frac{{U_*}^2 H_v}{2\nu} & z \geq H_v \end{cases} \tag{2.12}$$

Denoting the time-mean stream-wise velocity in the uniform layer ($z \geq H_v$) as U_o, the local friction velocity U_* can be calculated from Eq. 2.12.

$$U_* = \sqrt{\frac{2\nu U_o}{H_v}} \tag{2.13}$$

In this study, we use laboratory measurement to examine the validity of Eq.2.13 and to look for connections between H_v and the characteristics of the model canopy. In addition, we evaluate the relationship between the local estimate of U_*, denoted in Eq.2.13, and the effective friction velocity (U_{*eff}) associated with the spatially-averaged bed shear stress.

Chapter 3

Methods

3.1 Experimental set up

Laboratory experiments were conducted in a horizontal recirculating glass flume with a 1.2m-wide and 13m-long test section (bed slope $s_b = 0$). By varying the weir height at the end of the flume, the water depth was varied between $H = 0.07m$ and $H = 0.13m$. By varying the pump frequency, the cross-sectional average velocity was varied between 0.002 and 0.18 m/s. A backscatter Laser Doppler velocimetry (LDV) probe (Dantec Dynamics) was mounted on a manually driven positioning system. Simultaneous measurements of stream-wise (u) and vertical (w) velocity were recorded over a 300s period. The positioning system allowed the LDV to move in both the z and y directions with a resolution of 0.1mm. In order to measure velocity very close to the bed, the LDV axis was tilted 1 deg from horizontal and the velocity was later corrected for this tilt. The wavelengths of the two beams of the LDV were 514.5 and 488nm, and the focal length was 399mm. For the majority of positions the sampling frequency was $125Hz$, but close to the bed the sampling frequency dropped as low as $5Hz$. At this frequency, the mean velocity was still reliably measured, but not the Reynolds stress. In these cases the near bed Reynolds stress measurements were excluded from further anlayses, as noted below. The sampling volume was $4mm \times 0.2mm \times 0.2mm$ in the y, x, and z direction, respectively. The flow was seeded with pliolite particles, and because the PVC board on the bottom of the flume

is black, the reflection from the bed was negligible.

To simulate emergent vegetation, rigid dowels were placed in a staggered array in perforated, black, PVC baseboards with smooth surfaces. The dowels covered the full width of the flume. Two cylinder sizes were considered, with diameter $d = 0.0063m$ and $d = 0.0126m$. The frontal area per unit volume ranged from $a = 0.5m^{-1}$ to $17.8m^{-1}$. The drag coefficient for the cylinders in the array, C_D, was estimated from a previous study [99]. 20 trials with dowels and 4 with a bare channel were conducted (Table 3.1). For each trial, the velocity was measured at 15 to 40 positions along 3 to 11 vertical profiles, with at least 4 profiles for a vegetated channel. Our experiments have shown that in a canopy 4 profiles give a good estimation of the laterally-averaged parameters if the profiles are recorded at the extrema of the velocity field (i.e one profile just behind a dowel $y/ds = 0$, one profile behind the closer adjacent dowel in the upstream row $y/ds = 1$, one profile at the maximum velocity between the two previous dowels $y/ds = 0.5$, and one profile between the maximum velocity and the minimum velocity $y/ds = 0.25$). The vertical spacing of measurements was 0.2mm near the bed. For the denser canopies ($a = 12.6m^{-1}$ and $17.3m^{-1}$), 2 or 3 dowels at the side of the flume were removed to clear the optical path. Because the cylinders were removed from positions laterally adjacent to the measurement point, their removal did not alter the flow development leading up to the measurement point. Details about each trial can be found in Table 3.1. Due to the constraint of optical access, the individual vertical profiles were positioned along a lateral transect mid-way between rows. The transect is shown in Fig.3-1b.

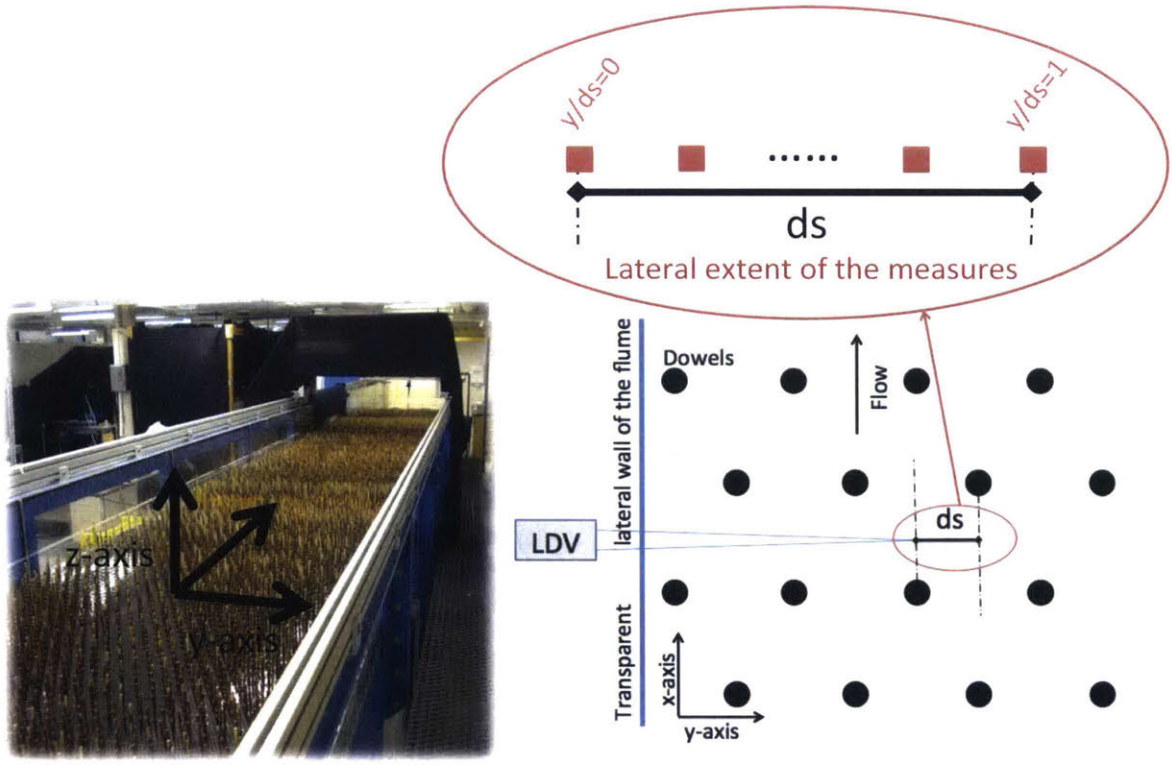

Figure 3-1: Experimental set-up. The LDV measured streamwise (u) and vertical (w) velocity. Vertical profiles were recorded at different lateral positions along the transect of length ds (shown above) positioned at the mid-point between two rows of wood dowels.

Table 3.1: Experimental conditions for 24 trials

	Stem diameter $d[m]$	Density $a[m^{-1}]$	Spacing $ds[m]$	Average velocity U $[m/s]$	Water depth H$[m]$	Nb. of profiles (Meas. per profile)
Bare Channel						
Case 1.1	NA	0	NA	0.047	0.083	4 (40)
Case 1.2	NA	0	NA	0.091	0.094	3 (20)
Case 1.3	NA	0	NA	0.036	0.110	4 (39)
Case 1.4	NA	0	NA	0.088	0.124	3 (28)
Emergent vegetation						
Case 2.1	0.0063	0.5	0.056	0.013	0.075	11 (32)
Case 2.2	0.0063	0.5	0.056	0.093	0.098	7 (19)
Case 2.3	0.0063	0.5	0.056	0.050	0.078	9 (28)
Case 2.4	0.0063	0.5	0.056	0.048	0.114	5 (22)
Case 3.1	0.0063	4.3	0.019	0.052	0.097	11 (30)
Case 3.2	0.0063	4.3	0.019	0.083	0.120	7 (21)
Case 3.3	0.0063	4.3	0.019	0.016	0.098	5 (18)
Case 3.4	0.0063	4.3	0.019	0.036	0.117	5 (18)
Case 4.1	0.0063	17.3	0.010	0.054	0.095	7 (23)
Case 4.2	0.0063	17.3	0.010	0.010	0.082	5 (20)
Case 4.3	0.0063	17.3	0.010	0.081	0.104	7 (18)
Case 4.4	0.0063	17.3	0.010	0.047	0.111	5 (17)
Case 5.1	0.0126	2.9	0.033	0.046	0.087	5 (18)
Case 5.2	0.0126	2.9	0.033	0.099	0.098	4 (19)
Case 5.3	0.0126	2.9	0.033	0.041	0.117	4 (16)
Case 5.4	0.0126	2.9	0.033	0.002	0.075	4 (21)
Case 6.1	0.0126	12.6	0.016	0.143	0.117	9 (21)
Case 6.2	0.0126	12.6	0.016	0.098	0.100	5 (18)
Case 6.3	0.0126	12.6	0.016	0.020	0.084	6 (16)
Case 6.4	0.0126	12.6	0.016	0.176	0.074	4 (15)

Case 4.4 has been excluded from our analysis because significant surface waves were observed in this case. The average velocity, U, is calculated as the average of the individual depth-average for each profile.

3.2 Data analysis

In this paper, a spatial-average ($\langle\ \rangle$) denotes the lateral-average along this particular transect. The friction velocity estimated from the spatially-averaged velocity is denoted $\langle U \rangle_*$, and the spatial-average of the local estimates of friction velocity U_*, i.e. based on individual velocity profiles, is denoted $\langle U_* \rangle$. The relationship among $\langle U \rangle_*$, $\langle U_* \rangle$ and U_{*eff} is discussed in the results and discussion section.

The measured velocities were used to estimate the friction velocity by fitting the Law of the Wall (Eq.2.8), and the new linear stress model (Eq.2.10 and 2.12). For the Law of the Wall, U_* was used as the fitting parameter, and the best fit was chosen based on the minimum value of the sum-of-squares error (SSE) between the measurements and the model for both $Z_+ \leq 5$ and $Z_+ \geq 30$ region, i.e. the two regions were fitted together in a single procedure. The uncertainty in the fit was evaluated by finding the range of U_* values that return SSE less than the standard deviation amongst the individual measured profiles. For the new linear stress model, both U_* and H_v were used as fitting parameters for Eq.2.12 with the best combination of values returning the lowest SSE. The uncertainty of U_* and H_v were tuned separately using the same method as the Law of the Wall. Correspondingly, $\langle U \rangle_*$ and H_{vo} were estimated by fitting Eq.2.12 to the spatially-averaged velocity profile following the same procedure. Finally, for the bare channel cases, the friction velocity was also estimated by fitting Eq.2.7 over $Z_+ \geq 30$, which we call the total stress method. U_* was chosen based on the minimum SSE between $\rho U_*^2(1 - z/H)$ and $\left(\tau_{xz}^{Rey} + \tau_{xz}^{vis}\right)|_z$ with the stresses estimated from measured velocity data (Eq.2.3). At $Z_+ \leq 30$, $\left(\tau_{xz}^{Rey} + \tau_{xz}^{vis}\right)|_z$, oscillates intensely with the adjacent value differing by up to 20%. We therefore exclude data from $Z_+ \leq 30$ from the fit. The uncertainty of U_* was then determined from the range of U_* that return a SSE less than the spatial variation between individual local total stress ($\left(\tau_{xz}^{Rey} + \tau_{xz}^{vis}\right)|_z$) profiles. For convenience, the spatially-averaged value were used in all the fittings for bare channel cases, because of the homogeneity of the flow.

Chapter 4

Results

4.1 Linear distribution of near-bed viscous stress

Flow over a smooth bare channel

We first consider the smooth bare channel case. The vertical distribution of normalized spatially-averaged stresses and stream-wise velocity are shown in Fig. 4-1 for case 1.1. The data for all the figures in this section are listed in the appendix. The U_* obtained from the total stress method is used in the normalization. Near the bed ($z_+ \leq H_{v+}$), the viscous stress (triangles) had a linear distribution, supporting the linear stress model described above. For $z_+ = zU_*/\nu \leq 5$ the Law of the Wall and the linear stress model did equally well in describing the measured velocity (compare red and green curves in Fig.4-1b). However, unlike the Law of the Wall, the linear stress model also represented the measured velocity for $z_+ \geq 5$, up to $z_+ \approx 25$. That is, the new linear stress model provides a description of the velocity profile that extends through the buffer layer ($5 < Z_+ < 30$).

For the bare channel conditions, three methods were used to estimate the bed shear stress: the Law of the Wall (Eq. 2.8), the total stress method (Eq.2.7), and the new linear stress model (Eq. 2.10). The bed shear stress estimated from the Law of the Wall and the linear stress method agreed within uncertainty (Table 4.1) for cases 1, 2 and 3, and differed by only 14% for case 4. This agreement makes sense,

because near the wall ($Z_+ < 5$), the velocity profiles associated with each fit essentially overlap (Fig. 4-1b). The total-stress method also produced values of U_* in agreement (within uncertainty) with the two velocity laws, providing a consistency check for the estimated U_*. Finally, the non-dimensional linear-stress layer height, $H_{v+} = H_v U_*/\nu$ (using U_* from the new linear stress model), had a consistent value across all four cases (within uncertainty), suggesting that $H_{v+} = 22 \pm 3(SD)$ may be a universal constant, although further verification is required. Since H_v is a close relative of the viscous sublayer thicknes, it is not surprising that it may have a universal value.

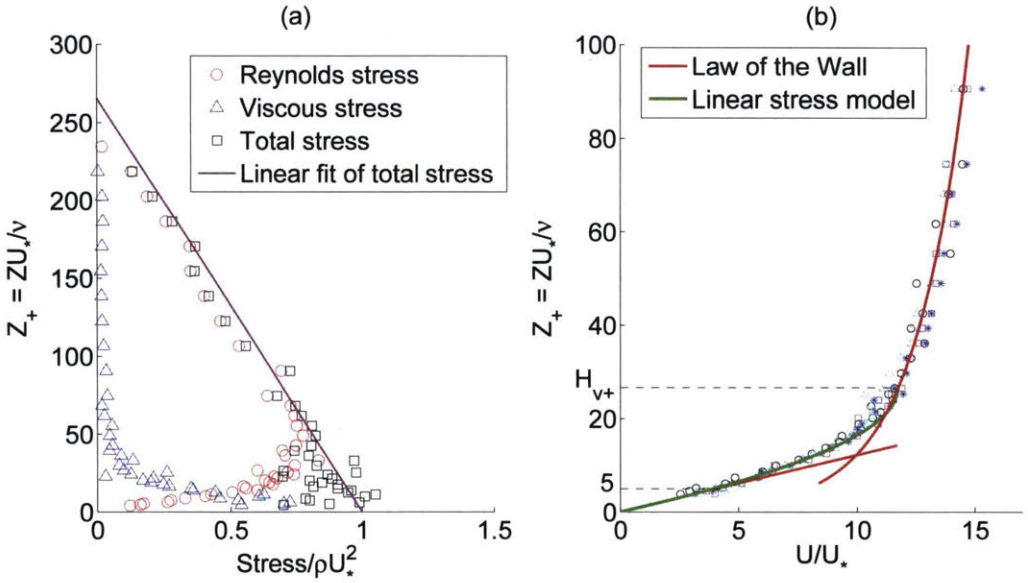

Figure 4-1: (a) Spatially-averaged stresses normalized by ρU_*^2 with U_* estimated from the total stress method, and (b) stream-wise velocity normalized by U_* at four horizontal locations (symbols) for case 1.1. The four locations are 5cm apart along a lateral transect in the middle of the flume. The near-bed viscous stress follows a linear distribution. The linear fit to the total stress (magenta line) represents the total stress method for U_* in Table 3.1. The time averaged stream-wise velocity profiles at four lateral positions are presented by four different symbols in figure (b). The velocity follows the Law of Wall (red curves in b) in the near bed region and the upper log-layer region. The new linear stress model (green parabola) follows the measured velocity up to $z = H_{v+} \approx 25$.

Table 4.1: The friction velocity U_* estimated from three different methods

Bare channel cases	Depth -averaged U$[m/s]$	Total stress method $U_*[m/s]$	Law of the Wall method $U_*[m/s]$	Linear-stress method	
				$U_*[m/s]$	$H_{v+} = \frac{H_v U_*}{\nu}$
Case1.1	0.047	0.0032 ± 0.0001	0.0029 ± 0.0001	0.0030 ± 0.0001	25 ± 4
Case1.2	0.091	0.0057 ± 0.0002	0.0052 ± 0.0003	0.0060 ± 0.0005	19 ± 4
Case1.3	0.036	0.0023 ± 0.0001	0.0023 ± 0.0002	0.0024 ± 0.0003	23 ± 6
Case1.4	0.088	0.0054 ± 0.0002	0.0048 ± 0.0002	0.0056 ± 0.0004	20 ± 3

U_* estimated from three different methods agree within uncertainty. The non-dimensional linear-stress layer height $H_{v+} = 22 \pm 3$ for the bare channel cases we studied.

Flow over smooth channels with emergent vegetation

Compared with the bare channel cases, the distribution of stresses within the emergent canopy was more complicated because two additional components were added by the canopy: the dispersive stress and the vegetative drag (Fig.4-2a). The vegetative drag, estimated by Eq.2.5, represented 97% of the total drag and dominated the flow resistance over the entire water column. Because the total stress is dominated by vegetation drag, the total stress normalized by the bed shear stress, $\rho \langle U \rangle_*^2$, is much larger than 1 at the bed. The vertical profiles of viscous stress at eleven positions within the array are shown in Fig.4-2b. Although the velocity varied spatially inside the canopy (Fig.4-3 and 4-4a), the viscous stress had almost no variation along the measurement transect. This gives support to the assumption made above that our transect represents a region of the flow for which the viscous stress distribution is dominated by the proximity to the bed, because the distance to the bed is smaller than the distance to the nearest stem. Further, the viscous stress was linear near the bed and zero in the upper layer (Fig.4-2b), which agreed with the linear stress model given in Eq.2.11. The dispersive stress and the Reynolds stress, though comparable to the viscous stress near the bed, reduce to zero at the bed, so the bed shear stress equals to the viscous stress at the bed, i.e. the normalized viscous stress goes to 1(Fig.4-2c).

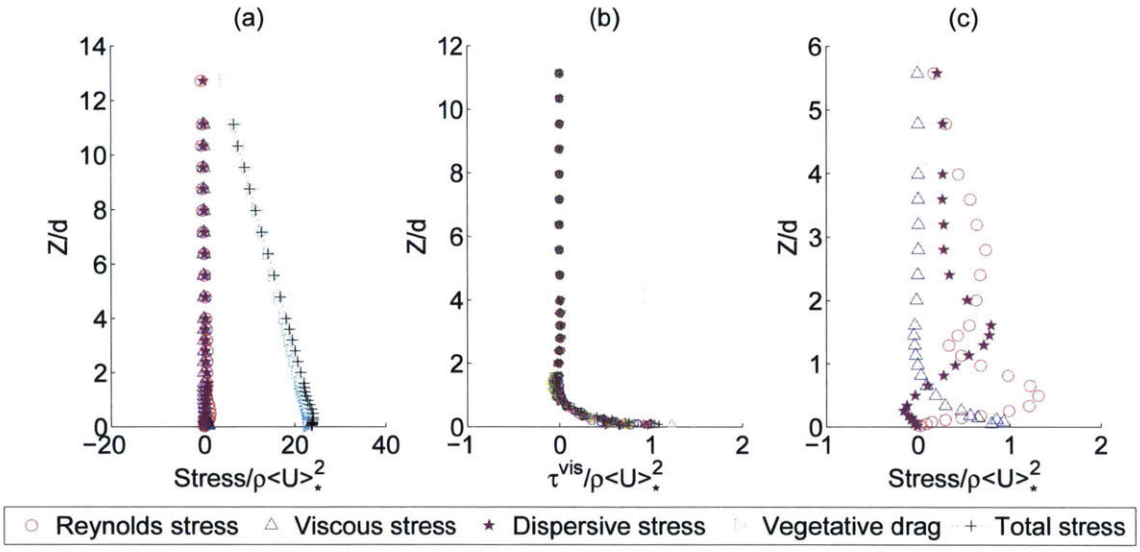

Figure 4-2: Emergent canopy case 3.1, $a = 4.3m^{-1}$, $ds = 3d$, $U_p = 0.052m/s$. The stem diameter for this case is 0.0063m, and the fitted linear-stress layer thickness $H_v = 0.0035m$, corresponding to $H_v/d = 0.56$. The vertical axis is the distance from the bed normalized by the stem diameter, and the horizontal axes are the stresses normalized by $\rho \langle U \rangle_*^2$, the bed shear stress fitted from the spatially-averaged velocity profile. (a) The spatially averaged stress distribution is shown with the vegetative drag calculated with Eq. 2.5 using drag coefficients C_D estimated from a previous study by [99]. Because the total stress is dominated by vegetation drag, the total stress normalized by the bed shear stress, $\rho \langle U \rangle_*^2$, is much larger than 1 at the bed. (b) Viscous stress profiles measured at 11 horizontal positions (symbols). (c) Spatially averaged stresses.

The individual vertical profiles of time-averaged, stream-wise velocity normalized by $\langle U \rangle_*$ at 11 lateral positions are shown in Fig. 4-3. Here $\langle U \rangle_*$ was derived from the fit of the linear-stress model (Eq.2.12) to the spatially-averaged velocity profile. At each lateral position, the velocity confirmed the two-zone profile proposed in Eq. 2.12. Specifically, the velocity was vertically uniform in the upper canopy ($z/d \geq 4$), and the velocity near the bed ($z/d < 0.5$) was parabolic (green curve in Fig. 4-3b).

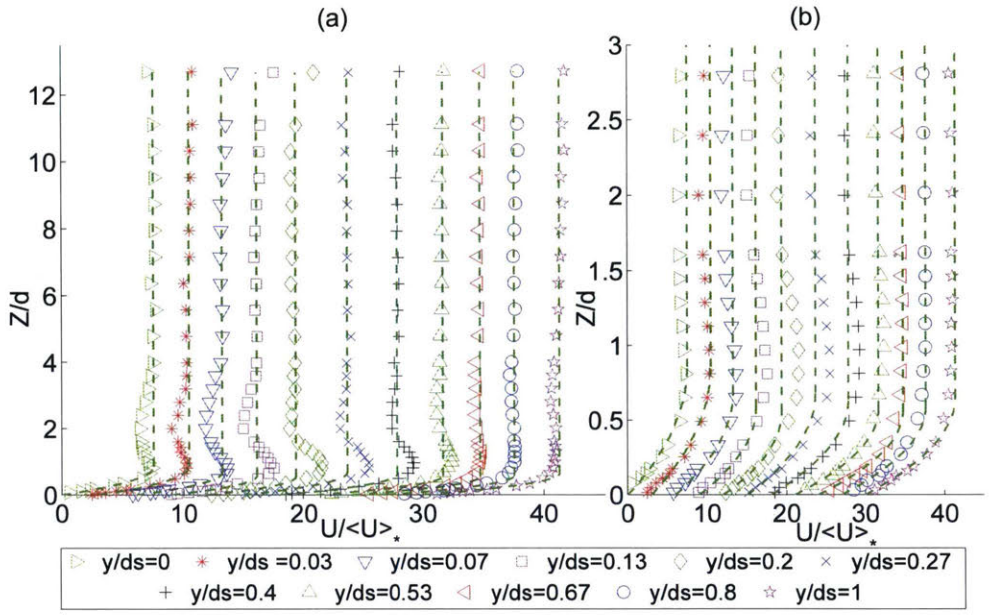

Figure 4-3: Case 3.1 (as in Fig.4-2). Vertical profiles of time-mean stream-wise velocity normalized by $\langle U \rangle_*$ at 11 horizontal positions (symbols). The x-axis of each profile is offset by 3 units. The green dashed curves represents the fit of the linear-stress model (Equation 11) to each individual profile. (a) The velocity distribution over the whole water depth. In the upper layer, the velocity is vertically uniform. (b) The velocity distribution in the near bed region. The velocity is parabolic very close to the wall.

The spatially-averaged time-mean velocity (the black curve in Fig. 4-4) also supported the linear stress model, i.e. the spatially-averaged velocity was vertically uniform in the upper canopy ($z/d \geq 4$) and parabolic in the near-bed region ($z/d \leq (H_{vo})/d$). Here H_{vo} was derived from the fit of the linear-stress model (Equation 11) to the spatially-averaged velocity profile, the same as $\langle U \rangle_*$. Note again how the parabolic velocity profile provided a good fit to the spatially-averaged velocity over a larger distance (up to $Z_+ = H_{vo} \langle U \rangle_* / \nu = 19$) than the Law of the Wall, which is only valid up to $Z_+ = 5$. However, similar to measurements described in [50] a region of velocity deviation was observed close to $Z_+ = H_{vo+}$. The Reynolds stress exhibited a local maximum at the same distance above the bed (circles, Fig. 4-2c). The feature deteriorates with increasing lateral distance from the upstream cylinder (Fig.4-3) suggesting it is associated with the horseshoe or junction vortex formed at the bed near each cylinder base (see Fig.7 in [93]). These coherent structures scale with the cylinder diameter.

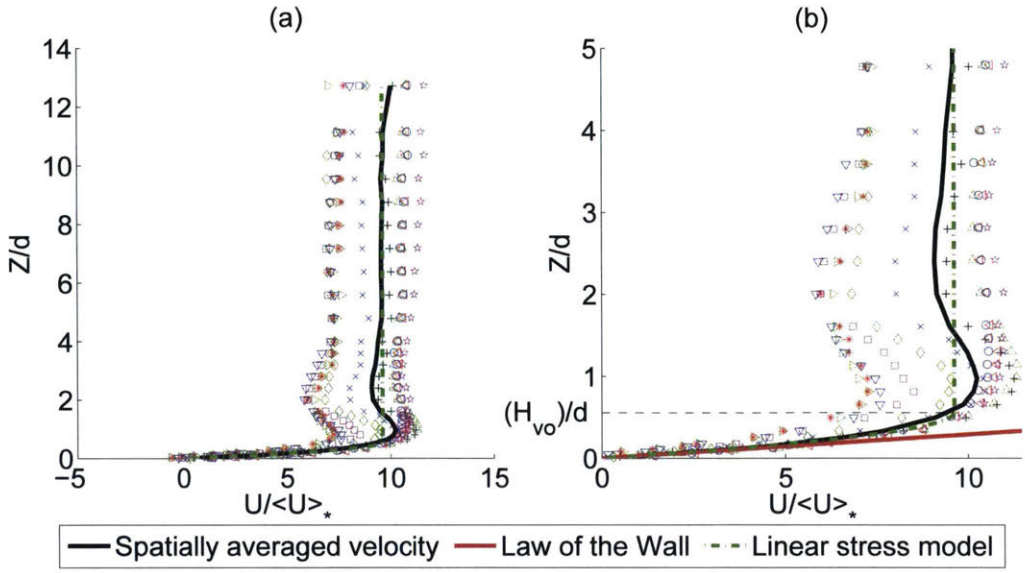

Figure 4-4: Case 3.1. Vertical profiles of time-mean stream-wise velocity normalized by $\langle U \rangle_*$ at 11 horizontal positions (symbols shown in Fig.4-3) and the spatial-average (shown with heavy black curve). The green dashed curve represents the fit of the linear-stress model (Equation 11) to the spatially-averaged velocity profile. The red line represents the fit of the linear part of the Law of the Wall (Equation 7) to the spatially-averaged velocity. (a) In the upper layer, the spatially-averaged velocity is constant except in regions very close to the surface. (b) The distribution of the spatially-averaged velocity in the near bed region is parabolic up to $H_{vo}/d \approx 0.5$.

We next consider the relationship between $\langle U \rangle_*$ and H_{vo}, fitted from the spatially-averaged velocity, and the locally fitted U_* and H_v (Fig.4-5). Along the lateral transect (defined in Fig.3-1), the local friction velocity $U_*(y)$ is fairy uniform, varying by a maximum of 30% from $\langle U \rangle_*$. The minimum $U_*(y)$ occurred directly behind the upstream dowel ($y = 0$), which is reasonable because the velocity is also minimum here. The spatial-average of the local U_*, denoted as $\langle U_* \rangle$, is approximately equal to $\langle U \rangle_*$ (within 10% uncertainty). To conclude, Fig.4-3, 4-4 and 4-5 take together, have shown that along the measurement transect, the new linear stress model (Eq.2.11) fits both the local velocity profiles and the spatially-averaged profile. In addition, despite the variation in upper-water column velocity (U_o) across the transect (Fig.4-4), the friction velocity was fairly constant, such that either order of averaging and fitting ($\langle U \rangle_*$ versus $\langle U_* \rangle$) produced similar values.

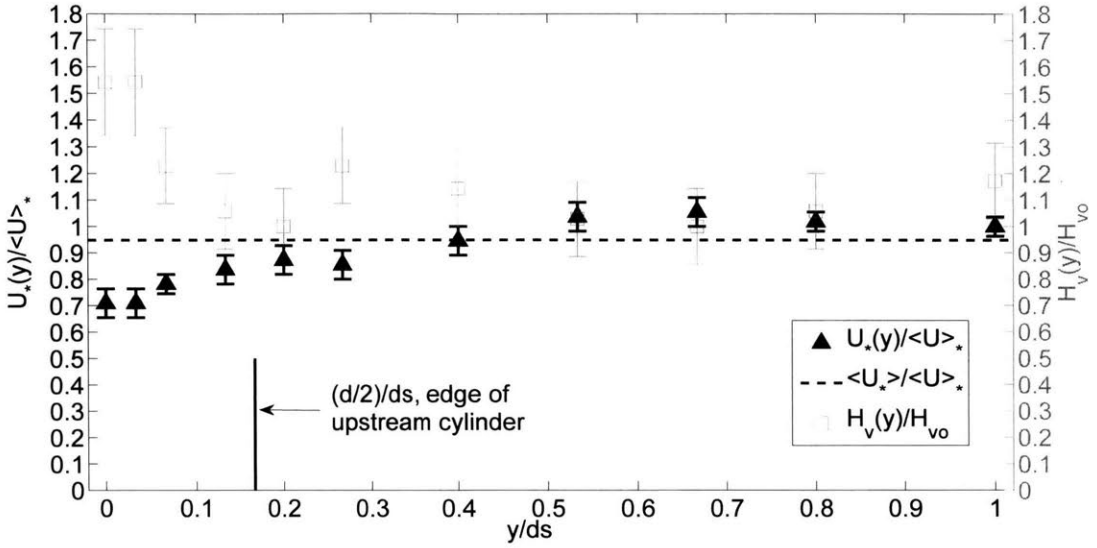

Figure 4-5: Case 3.1. The distribution of the $U_*(y)$, fitted from local velocity profile, normalized by $\langle U \rangle_*$ (triangles), and the distribution of the locally fitted $H_v(y)$ normalized by H_{vo} (squares). Here y indicates the position in the lateral transect, with $y = 0$ right behind the dowels as shown in Fig. 3-1. The bold black dashed line represents the spatial-average of local $U_*(y)$ normalized by $\langle U \rangle_*$.

In the following sections we focus on developing an estimator for $\langle U \rangle_*$. More discussions on how $\langle U \rangle_*$ or $\langle U_* \rangle$ can be used to estimate the effective friction velocity at the canopy scale is presented in the discussion section.

4.2 The scale of H_{vo}

The scale of H_{vo} at low Re_H for $a \geq 4.3m^{-1}$

The values of H_{vo} determined from the linear stress model fit to the spatially-averaged velocity are plotted in Fig.4-6. Subplot (a) and (b) separate the cases by cylinder diameter, $d = 6.3$ and $12.6mm$, respectively. First, let us consider the smaller cylinder size (Fig.4-6a). When the array had sufficient density ($a = 4.3m^{-1}$ and $17.3m^{-1}$, shown with red symbols), H_{vo} was comparable to the stem radius (shown by horizontal dashed line). If the depth Reynolds number was not too high ($Re_H \leq 6000$), at similar values of Re_H, H_{vo} in the sparse canopy (black symbols) and the bare channel (open symbols) were clearly larger than the stem radius. Therefore the presence of a dense

canopy ($a \geq 4.3m^{-1}$) reduced the linear-stress layer thickness to a scale comparable to $d/2$ for small depth Reynolds number (e.g. $Re_H < 6000$). For simplicity, $R = d/2$ is used in the following paragraphs. However, in sparse canopies ($a = 0.5m^{-1}$ in Fig.4-6a, black symbols), H_{vo} was larger than the stem radius R. Specifically, the sparse canopy value of H_{vo} was between the bare channel value and the value in a dense canopy (R). We propose that at low depth Reynolds number (e.g. $Re_H < 6000$), for canopies of sufficient density (here $a \geq 4.3m^{-1}$), the viscous sub-layer is restricted to the scale of the cylinder radius. The relationship between H_{vo} and R observed for dense canopies ($a \geq 4.3m^{-1}$) is likely associated with the coherent structures formed near the base of each stem. These structures create strong vertical velocity near the bed, as shown by [93]. In particular, Fig.5 in [93] shows strong vertical velocity occurs near $z = R$. By enhancing vertical momentum transport near the bed, the coherent structures may suppress H_{vo} to a scale comparable to R.

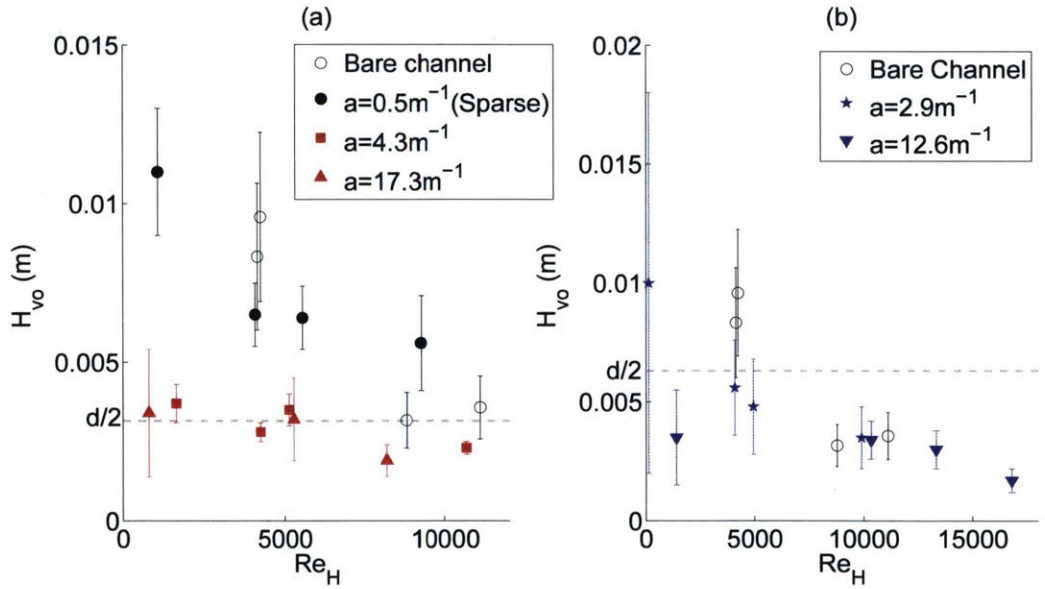

Figure 4-6: The linear-stress layer thickness, H_{vo}, versus depth Reynolds number, Re_H, for the bare channel cases (open circles) and the vegetation cases (a) with stem diameter d=6.3 mm and (b) with stem diameter d=12.6mm. The depth Reynolds number Re_H is calculated using the spatially-averaged upper-layer velocity $\langle U_o \rangle$ for the vegetated cases and the spatial-average of the depth-averaged velocity for the bare channel cases. The vertical error bars represent the uncertainty in fitting H_{vo}.

Dependence on Re_H

As Re_H increased, the bare channel values of H_{vo} decreased (Fig.4-6a), which is consistent with the constant value observed for $H_{vo+} = (H_{vo} \langle U \rangle_*)/\nu = 22 \pm 3$ (Table 4.1). As $\langle U_o \rangle$ increases, $\langle U \rangle_*$ also increases, so that H_{vo} decreases. The same trend is observed for the viscous sub-layer defined by the Law of the Wall (δ_s), i.e. $\delta_{s+} = 5$, so that as $\langle U_o \rangle$ increases, δ_s decreases. In our study, H_{vo} in the bare channel became comparable to the smaller stem radius ($d = 6.3mm$) near $Re_H = 8000$ (Fig.4-6a), so that above this value of Re_H, the presence of the canopy has little impact on the value of H_{vo}. Although not evident in the cases we tested, we conjecture that if Re_H was increased further ($Re_H > 8000$), the bare channel H_{vo} would become smaller than R. Accordingly, we posit that there exists a Reynolds number above which the linear-stress layer thickness, H_{vo}, would be the same in both bare and vegetated channels, because the constraint imposed on H_{vo} by bed-generated turbulence would be greater than the constraint imposed by the stem-generated turbulence.

Now, let us consider the larger size cylinders ($d = 12.6mm$, Fig.4-6b). The values of H_{vo} observed with the larger diameter arrays were consistent with conclusions drawn above based on the smaller diameter arrays. Because the size constraint imposed by the stem radius was larger ($R = 6.3mm$), the bare channel value of H_{vo} became comparable to R at a lower Re_H than occurred with the smaller radius arrays ($R \approx 3.2mm$). Specifically, the bare and vegetated channel values of H_{vo} became comparable to one another at $Re_H = 4000$. At higher Re_H, there was no difference between the bare channel and emergent array conditions. To summarize, below a transition Re_H, a dense canopy ($a \geq 4.3m^{-1}$) can suppress H_{vo} to R, but at higher Re_H, H_{vo} is the same in both bare and vegetated channels. The transition Re_H decreases with increasing stem radius. Based on this, we suggest that the linear-stress layer thickness in a dense canopy ($a \geq 4.3m^{-1}$) will be $H_{vo} = min\,(R, 22\nu/\langle U \rangle_*)$, where the later term denotes the value for a bare bed.

The fitted H_{vo} normalized by $min\,(R, 22\nu/\langle U \rangle_*)$ are shown in Fig.4-7. For the bare channel and emergent channels with $a \geq 4.3m^{-1}$, the model gives a very robust

prediction of H_{vo}, with these cases falling along the line of model agreement, shown by the horizontal dashed line. The proposed model for H_{vo} fails for sparse arrays ($a = 0.5m^{-1}$, gray circles).

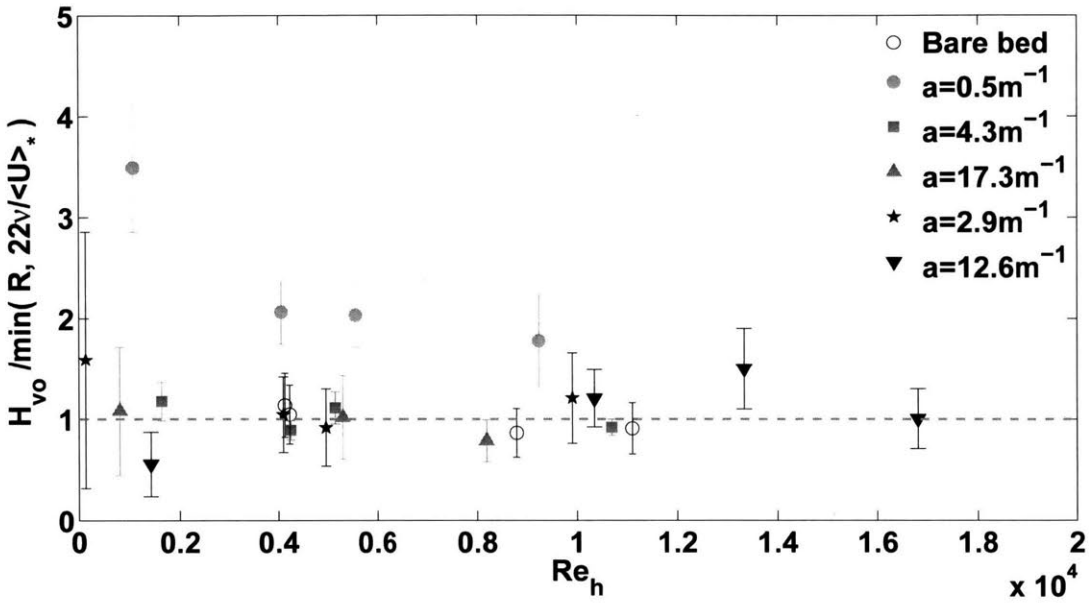

Figure 4-7: The fitted H_{vo} normalized by the proposed model $min\left(R, 22\nu/\left\langle U\right\rangle_*\right)$. The dashed line indicates agreement with the proposed model. The vertical errorbars represent the fitting errors of H_{vo} normalized by $min\left(R, 22\nu/\left\langle U\right\rangle_*\right)$.

4.2.1 Estimation of $\langle U\rangle_*$ in an emergent canopy

As shown in Fig.4-4, the spatially-averaged velocity can also be fit to Eq.2.13, producing the estimate $\langle U\rangle_* = \sqrt{\frac{2\nu\langle U_o\rangle}{H_{vo}}}$. When the scaling $H_{vo} = d/2$ is appropriate, we propose that the friction velocity $\langle U\rangle_* = 2\sqrt{\frac{\nu\langle U_o\rangle}{d}}$. As discussed above, this scaling fails if the canopy is too sparse, such that the stem-scale coherent structures do not dominate the near-bed flow, or if the depth Reynolds number is too high, such that the bed-driven turbulence places a stronger constraint on H_{vo} than the stem related turbulence. To reflect the influence of both bed-driven and stem-driven near-bed turbulence, we propose the following relationship for dense emergent canopies:

$$\langle U\rangle_* = max\left(\sqrt{C_f}\,\langle U_o\rangle\,, 2\sqrt{\frac{\nu\,\langle U_o\rangle}{d}}\right) \tag{4.1}$$

Here, C_f is the drag coefficient for the bare bed. Note that although $\langle U_o \rangle$ strictly defines the spatial-average of the velocity in the uniform upper layer of the canopy, in most cases $\langle U_o \rangle$ is close to the spatial-average of the depth-averaged velocity, which is denoted as the average velocity U in Table 3-1. Due to the repeatable pattern of the dowels in y direction, the spatial-average of the depth-averaged velocity along the lateral transect shown in Fig.3-1 is equal to the volume flow rate per unit cross-sectional area. So for the purpose of prediction, $\langle U_o \rangle$ may be taken as the volume flow rate per unit cross-sectional area corrected for porosity. Eq.4.1 captures the physical limit that at high Reynolds number the vegetation will have negligible influence on H_{vo} and $\langle U \rangle_*$. This limit is demonstrated in the values of $\langle U \rangle_*$ shown in Fig. 4-8a. For the two stem diameters we studied, when Re_H was higher than 8000, the non-dimensional friction velocity $\langle U \rangle_* / \langle U_o \rangle$ in the emergent canopy was close to the value observed in the bare channel, regardless of the stem diameter and the density of the canopy. However, at low and moderate depth Reynolds number, $\langle U \rangle_* / \langle U_o \rangle$ in dense canopies (red and blue symbols) was higher than bare channel values in Fig. 4-8a. Note that the transition Re_H should decrease as d increases. That is, for a larger stem diameter, the bare channel value of H_{vo} would reach R at a lower Re_H. We caution that the transition Re_H will likely also depend on the bare bed texture which influences C_f. The quantification of C_f, however, is not the focus of this study. Here we assume that C_f for the bare channel is already known, and concentrate on quantifying the bed shear stress once cylinder arrays have been added to the bare bed.

Finally, Fig. 4-8b depicts $\langle U \rangle_*$ non-dimensionalized by $\sqrt{(\nu \langle U_o \rangle)/d}$ for $Re_H \leq 6000$. Over this range of Re_H, $\langle U \rangle_* / \langle U_o \rangle$ was enhanced by dense canopies with stem diameter $d = 6.3mm$ (the red symbols in Fig. 4-8a). Compared with the scatter of $\langle U \rangle_* / \langle U_o \rangle$ over the same range of Re_H shown in Fig. 4-8a, the $\langle U \rangle_*$ non-dimensionalized by $\sqrt{(\nu \langle U_o \rangle)/d}$ was roughly a constant (≈ 2) as shown in Fig. 4-8b. This observation confirmed that for this range of conditions $\langle U \rangle_*$ might be estimated as $\langle U \rangle_* \approx 2\sqrt{(\nu \langle U_o \rangle)/d}$.

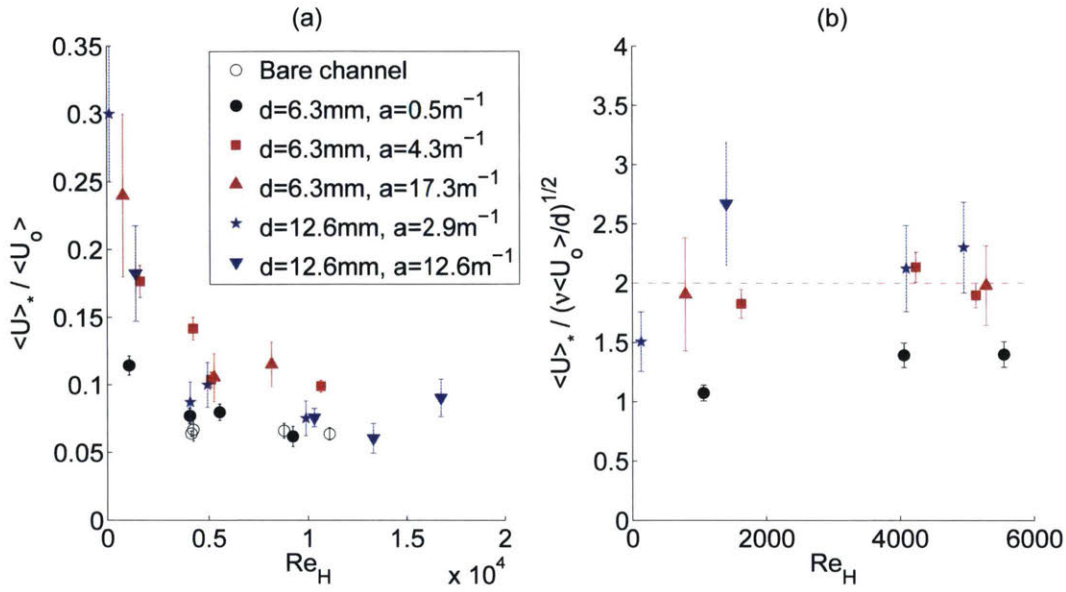

Figure 4-8: The fitted $\langle U \rangle_*$ non-dimensionalized by (a) $\langle U_o \rangle$ and (b) $\sqrt{(\nu \langle U_o \rangle)/d}$. The black symbol represents the sparse canopy ($a = 0.5m^{-1}$). In the bare channel with smooth bed (open symbols), $\langle U \rangle_* / \langle U_o \rangle \approx 0.06$.

In order to test the robustness of the conceptual model, the $\langle U \rangle_*$ obtained from Eq.4.1 normalized by $\langle U_o \rangle$ was plotted again the fitted $\langle U \rangle_*$ normalized by $\langle U_o \rangle$ in Fig.4-9. As shown in the figure, $\langle U \rangle_* / \langle U_o \rangle$ for the bare bed cases (open circles) collapse to a single point, indicating that $\langle U \rangle_* / \langle U_o \rangle$ is a constant for bare bed channels with the same bed texture. In the channels with model vegetation, however, $\langle U \rangle_* / \langle U_o \rangle$ has a wide range of values. The proposed model (Eq.4.1 and the dashed line in Fig.4-9) captures the variation of $\langle U \rangle_* / \langle U_o \rangle$ in an emergent canopy with density $a \geq 4.3m^{-1}$. For $a = 0.5m^{-1}$, however, the model over-predicts $\langle U \rangle_* / \langle U_o \rangle$. More extensive testing is needed to more precisely define the array density above which Eq.4.1 applies.

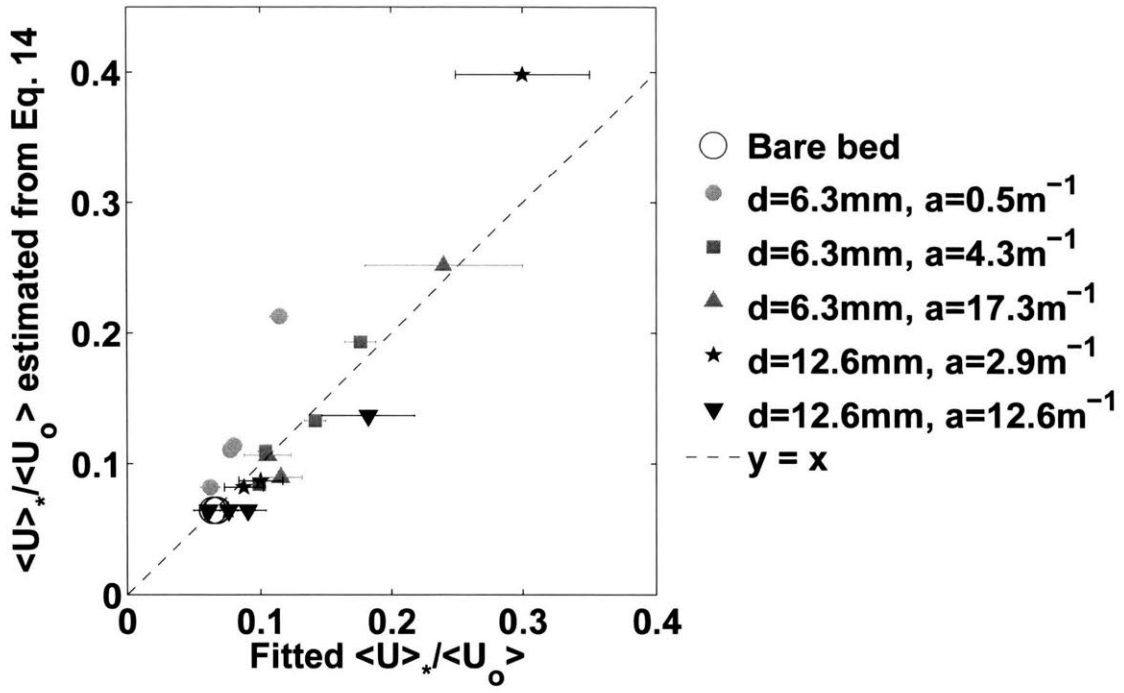

Figure 4-9: $\langle U \rangle_*$ obtained from Eq.14 normalized by $\langle U_o \rangle$ versus the fitted $\langle U \rangle_*$ normalized by $\langle U_o \rangle$. The open circles represent bare bed value also shown in Fig.4-8a. The size of the open circle, however, has been enlarged to make the data more distinguishable. The uppermost data point (black pentagram) corresponds to the case with the smallest Re_H as shown in Fig.4-8a.

Chapter 5

Discussion

5.1 Relationship between the measurement transect and the canopy average

As discussed in the results section, the friction velocity $\langle U \rangle_*$, fitted from the spatially-averaged velocity $\langle U \rangle$ along the measurement transect (Fig. 3-1), falls within 10% of $\langle U_* \rangle$, the spatial-average of the local U_* (Fig.4-5). In this section, we use the numerically simulated data from [83] to show that $\langle U_* \rangle$ may be a good approximation for the effective friction velocity U_{*eff} $(= \sqrt{\langle U_*^2 \rangle})$ within some uncertainty. The simulation results is shown in Fig.5-1.

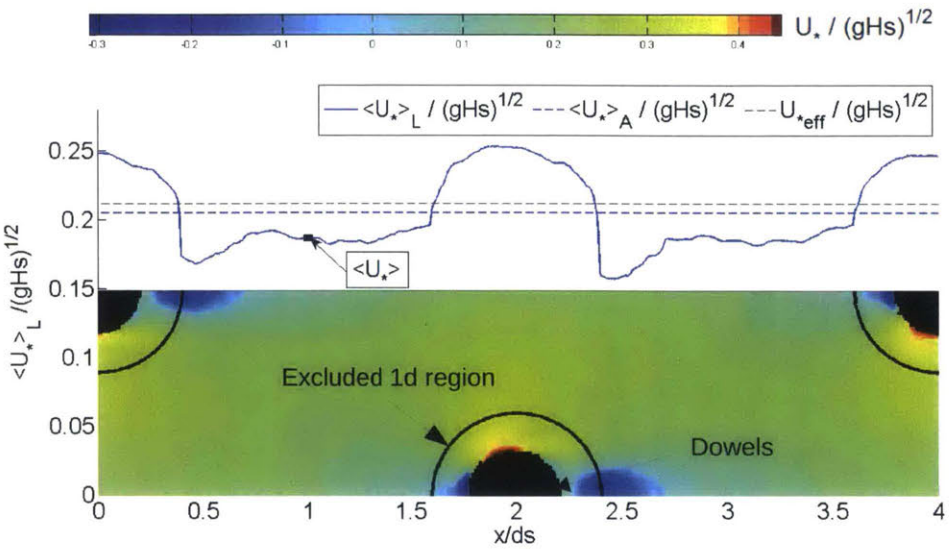

Figure 5-1: Estimates of bed shear stress normalized by the total stress, $\sqrt{gHs}$. Note that vegetative drag also contributes to the total stress, so that the normalized bed shear stress has an average value less than 1. The color map and color bar is adapted from Fig. 4 of [83]. In their simulation, the flow is from left to right through a staggered array of cylinders with ds (defined in Fig. 3-1) equal to $2.5d$. U_* is negative if the shear stress on the bed is in $-x$ direction. The depth Reynolds number Re_H is around 3000. The blue curve shows the lateral-average of the simulated $U_*/\sqrt{gHs}$ at each x position excluding 1 diameter region around the dowels. The effective friction velocity U_{*eff} is the black dashed line.

We first exclude the data in the region within one diameter from the center of each stem (Fig.5-1). We justify this exclusion based on the fact that we seek an estimate of bed shear stress for the future purpose of predicting net sediment flux through the canopy. The elevated (red) and diminished (blue) regions of bed stress close to the individual cylinders only produce localized sediment transport, i.e. the scour holes and deposition mounds classically observed near bridge piers (Fig.1 in [110]), and are not indicators of sediment flux at the canopy scale. Specifically, [40] observed that the generation of individual scour holes occurs at lower channel velocities than the onset of canopy-scale sediment transport. Rather, the value of bed shear stress within the contiguous region of relatively uniform bed shear stress (green region in the color map) represents the more relevant value for predicting canopy-scale sediment

transport.

After excluding data from within 1 diameter of each stem center, we laterally-averaged the local U_* at each x position (upper plot in Fig.5-1). This lateral-average of local U_* is denoted as $\langle U_* \rangle_L$. The position $x/ds = 1$ corresponds to the measurement transect used in this study, and this point is marked in Fig.5-1. The average of $\langle U_* \rangle_L$ along the x direction, denoted as $\langle U_* \rangle_A$, is the canopy-scale area average of U_*. Fig.5-1 shows the variation $\langle U_* \rangle_L$, normalized by the shear velocity associated with the total stress $\sqrt{gHs}$, along x (blue curve). Note that since vegetative drag also contributes to the total stress, this normalized bed shear stress has an average value less than 1. In the region between cylinders, e.g. $x/ds = 0.5$ to 1.5, $\langle U_* \rangle_L$ is relatively uniform, and close to $\langle U_* \rangle$ (marked in figure). Further, $\langle U_* \rangle$ differs from $\langle U_* \rangle_A$ (blue dashed line) by only 10%. For arrays with larger spacing between cylinders, the uniform region will occupy a larger fraction of the total area, and the difference between $\langle U_* \rangle$ and $\langle U_* \rangle_A$ will decrease. We therefore tentatively suggest that $\langle U_* \rangle$ is representative of the canopy-average. In addition, the effective friction velocity, defined as $U_{*eff} = \sqrt{\langle U_*^2 \rangle}$ (black dashed line Fig.5-1) is approximately equal to the $\langle U_* \rangle_A$ (within 5%). Given this, we suggest that Eq.4.1 may reasonably predict the effective friction velocity U_{*eff}:

$$U_{*eff} = max\left(\sqrt{C_f}\langle U_o \rangle, 2\sqrt{\frac{\nu \langle U_o \rangle}{d}}\right) \tag{5.1}$$

We caution that this conclusion is tentative, because [83] only provides maps of bed shear stress for a single case, $Re_H \approx 3000$ and $ds = 2.5d$.

5.2 Limitations of the model

The linear-stress model developed in this study has several limitations. Firstly, it only works when the frontal area per unit canopy volume a is large enough so that the velocity in the upper water column is uniform and that the stem generated turbulence is strong enough to limit the scale of H_v to R. In our experiments, we found that these conditions are met for $a \geq 4.3m^{-1}$.

Secondly, the vegetation center-to-center spacing ds should be larger than stem diameter d. As discussed in the theory section, within one diameter of the stem center, the local linear stress model does not hold because the horseshoe vortex system generated at the stem base locally alters the stress distribution. In addition, as the center-to-center spacing (ds) decreases below $2.5d$, the case shown in Fig.5-1, the region where $\langle U_* \rangle_L$ is uniform also decreases. As a result the difference between $\langle U_* \rangle$ and U_{*eff} would become larger, degrading the accuracy of the shear-stress estimate given in Eq.5.1. However, for $ds/d = 2.5$, the difference between $\langle U_* \rangle$ and U_{*eff} is only 15% (Fig.5-1), implying that Eq.5.1 is accurate to within 15%.

Thirdly, the model and experiments described here only consider smooth and impermeable beds. Using the distinction between hydraulically rough and smooth flows as a guide, we expect that the validity of the proposed model for rough beds would depend on the relative size of the bed roughness (sediment size) and thickness of the linear-stress layer. For example, in a salt marsh, $\langle U_o \rangle$ may be between 1 and $10cm/s$ and typical stem sizes are $d = 0.1$ to $1cm$, such that the thickness of the linear-stress layer $H_{vo} = min\left(R, 22\nu/\sqrt{C_f}\,\langle U_o \rangle\right)$ is on the order of mm, which is larger than the sediment size (on the order of 0.1mm). In this case the model developed for smooth beds may provide a reasonable estimate of U_*. In contrast, on a floodplain $\langle U_o \rangle$ may be $1m/s$ or higher and d is O($10cm$), so that H_{vo} is on the order of 0.1mm which is comparable to sediment size. In this case, the bed roughness extends beyond what we expect to be the linear-stress layer, and we expect that the bed roughness will alter near-bed dynamics. Possibly this adjustment may be accomplished with an adjustment to C_f to reflect the appropriate roughness, but a firm conclusion cannot be drawn until experiments are completed on rough, permeable beds.

It is important to note that the spatial-averaging discussed in this paper (and especially in the results section) was targeted only at bed shear stress. The relationships between local values and area-averages cannot be extended to other quantities, such as velocity or dispersive stress. In addition, the model here only considers emergent vegetation with cylindrical geometry. To apply the model for submerged vegetation, the frontal area index ah (h is the height of the vegetation) has to satisfy $ah \geq 0.3$

so that the turbulence generated at the top of the submerged canopy does not penetrate to the bed and affect the near bed stress distribution ([52]). For vegetation with non-uniform frontal area, $a(z)$, the velocity in the upper layer of the canopy will not be uniform, instead varying inversely with a in z direction [67]. In this case, the upper layer velocity $\langle U_o \rangle$ will need to be defined more carefully.

Chapter 6

Conclusion

This study developed a model that can predict the friction velocity in smooth channels with and without model emergent vegetation. In a bare channel, the model assumes that within a distance H_v from the bed, the Reynolds stress is negligible so that the viscous stress decreases linearly with increasing distance from the bed. The experimental data confirm the near-bed linear distribution of viscous stress and suggest a universal value for the non-dimensional layer thickness $H_{v+} = 22 \pm 3$. Within a model canopy of emergent cylindrical dowels, the linear stress distribution was observed in regions more than one diameter from the center of each dowel (Fig.4-3). For canopy density above $4.3m^{-1}$, the thickness of the linear stress layer was shown to be the minimum of the stem radius $(d/2)$ and the bare channel value $(22\nu/\langle U \rangle_*)$, such that the effective friction velocity can be estimate from $U_{*eff} = max\left(\sqrt{C_f}\langle U_o \rangle, 2\sqrt{\frac{\nu\langle U_o \rangle}{d}}\right)$. The effective friction velocity in an emergent canopy is therefore either larger than or equal to the bare channel value, for comparable depth-average velocity.

Appendix A

Tables

This section contains the data included in the figures.

Table A.1: Experimental data for Fig.4-1

$z\ (m)$	$\overline{u}\ (m/s)$ at Profile 1	$\overline{u}\ (m/s)$ at Profile 2	$\overline{u}\ (m/s)$ at Profile 3	$\overline{u}\ (m/s)$ at Profile 4	τ^{vis} (mm^2/s^2)	τ^{Rey} (mm^2/s^2)
0.0012	0.0081	0.0101	0.0128	0.0103	NaN	1.26
0.0014	0.0094	0.0126	0.0116	0.0141	5.53	1.65
0.0016	0.0102	0.0129	0.0138	0.0139	7.20	1.77
0.0019	0.0142	0.0151	0.0165	0.0162	7.44	2.69
0.0023	0.0155	0.0186	0.0187	0.0187	5.40	2.80
0.0027	0.0193	0.0191	0.0206	0.0206	4.70	3.34
0.0031	0.0211	0.0231	0.0209	0.0224	6.21	4.13
0.0035	0.0242	0.0246	0.0255	0.0248	6.40	4.35
0.0039	0.0259	0.0272	0.0279	0.0261	4.51	5.17
0.0043	0.0278	0.0286	0.0285	0.0291	3.65	6.15
0.0047	0.0297	0.0309	0.0295	0.0293	3.57	5.71
0.0051	0.0299	0.0314	0.0320	0.0312	2.74	5.61
0.0055	0.0325	0.0321	0.0320	0.0321	2.52	6.77
0.0059	0.0322	0.0326	0.0348	0.0330	2.05	6.63
0.0063	0.0341	0.0352	0.0322	0.0339	1.75	6.45

0.0067	0.0351	0.0344	0.0352	0.0341	2.13	6.94
0.0071	0.0339	0.0364	0.0361	0.0339	0.32	6.83
0.0075	0.0368	0.0343	0.0349	0.0348	1.29	7.60
0.0079	0.0362	0.0383	0.0366	0.0331	2.65	7.35
0.0083	0.0370	0.0370	0.0381	0.0355	1.02	6.16
0.0093	0.0380	0.0388	0.0379	0.0364	0.85	7.63
0.0103	0.0393	0.0386	0.0392	0.0379	1.37	8.56
0.0113	0.0412	0.0413	0.0404	0.0394	0.92	7.25
0.0123	0.0393	0.0417	0.0409	0.0395	0.46	7.14
0.0133	0.0409	0.0421	0.0422	0.0402	0.59	7.68
0.0153	0.0401	0.0434	0.0427	0.0421	0.48	7.96
0.0173	0.0447	0.0438	0.0428	0.0433	0.58	7.71
0.0193	0.0427	0.0456	0.0452	0.0442	0.27	7.62
0.0213	0.0444	0.0448	0.0449	0.0439	0.18	7.47
0.0233	0.0463	0.0469	0.0441	0.0444	0.38	6.55
0.0283	0.0464	0.0490	0.0470	0.0453	0.35	7.10
0.0333	0.0484	0.0491	0.0489	0.0490	0.25	5.45
0.0383	0.0512	0.0499	0.0495	0.0489	0.19	4.73
0.0433	0.0524	0.0521	0.0494	0.0494	0.17	4.09
0.0483	0.0522	0.0531	0.0504	0.0500	0.15	3.56
0.0533	0.0520	0.0534	0.0530	0.0490	0.20	3.54
0.0583	0.0528	0.0549	0.0528	0.0528	0.23	2.63
0.0633	0.0542	0.0562	0.0533	0.0542	0.20	1.92
0.0683	0.0550	0.0565	0.0550	0.0550	0.04	1.32
0.0733	0.0550	0.0550	0.0550	0.0550	NaN	0.20

1

[1]Because in the bare channel, the spatial heterogeneity is small, only spatially averaged viscous stress and Reynolds stress are listed for case 1.1. Because the centered difference method was used to calculate the viscous stress, no value of viscous stress were given for the lowest and highest positions.

Table A.2: Experimental data for Fig.4-2, corresponding to case 3.1.

$z\ (m)$	τ^{vis} (mm^2/s^2)	τ^{Rey} (mm^2/s^2)	τ^{Disp} (mm^2/s^2)
0.0001	0.00	0.78	-0.16
0.0003	24.31	2.88	-1.01
0.0005	28.15	4.66	-1.08
0.0007	25.93	9.13	-2.23
0.0009	19.86	14.51	-2.11
0.0011	17.24	20.68	-3.17
0.0016	14.34	30.03	-4.64
0.0021	9.07	36.66	-3.59
0.0031	5.93	39.68	-0.81
0.0041	2.91	36.96	3.29
0.0051	1.05	29.71	8.60
0.0061	-0.05	20.71	12.47
0.0071	-0.73	14.40	16.85
0.0081	-1.06	10.33	21.73
0.0091	-1.34	13.24	23.58
0.0101	-0.96	17.06	24.12
0.0126	-0.45	19.31	16.30
0.0151	-0.02	20.59	10.52
0.0176	0.21	22.42	8.62
0.0201	0.25	19.50	8.66
0.0226	0.13	17.38	8.19
0.0251	0.17	13.48	8.31
0.0301	0.11	9.35	8.42
0.0351	-0.01	5.44	6.54
0.0401	-0.01	2.06	4.44
0.0451	0.02	-3.80	2.93

0.0501	0.04	-6.74	1.77
0.0551	-0.03	-7.81	-0.88
0.0601	0.01	-6.64	-1.33
0.0651	0.07	-12.49	-2.44
0.0701	0.14	-6.89	-0.30
0.0801	0.00	-14.99	-2.27

2

Table A.3: Experimental data for Fig.4-2 and 4-4, corresponding to case 3.1.

$z\ (m)$	$\overline{u}\ (m/s)$ at $y/ds = 0$	$\overline{u}\ (m/s)$ at $y/ds = 0.03$	$\overline{u}\ (m/s)$ at $y/ds = 0.07$	$\overline{u}\ (m/s)$) at $y/ds = 0.13$	$\overline{u}\ (m/s)$ at $y/ds = 0.2$	$\overline{u}\ (m/s)$ at $y/ds = 0.27$
0.0001	-0.0032	-0.0031	-0.0014	-0.0005	0.0018	0.0009
0.0003	-0.0006	-0.0005	0.0009	0.0023	0.0072	0.0056
0.0005	0.0032	0.0029	0.0065	0.0076	0.0109	0.0097
0.0007	0.0086	0.0076	0.0088	0.0141	0.0164	0.0143
0.0009	0.0123	0.0121	0.0128	0.0177	0.0196	0.0187
0.0011	0.0146	0.0142	0.0150	0.0201	0.0241	0.0237
0.0016	0.0229	0.0227	0.0245	0.0252	0.0309	0.0316
0.0021	0.0271	0.0272	0.0296	0.0301	0.0356	0.0388
0.0031	0.0358	0.0343	0.0378	0.0394	0.0450	0.0490
0.0041	0.0390	0.0387	0.0418	0.0443	0.0507	0.0554
0.0051	0.0401	0.0400	0.0418	0.0468	0.0521	0.0576
0.0061	0.0386	0.0399	0.0411	0.0453	0.0524	0.0573
0.0071	0.0377	0.0390	0.0390	0.0440	0.0509	0.0554
0.0081	0.0361	0.0371	0.0365	0.0424	0.0479	0.0534
0.0091	0.0356	0.0372	0.0352	0.0400	0.0445	0.0521
0.0101	0.0352	0.0358	0.0345	0.0378	0.0413	0.0479
0.0126	0.0348	0.0329	0.0321	0.0329	0.0376	0.0443
0.0151	0.0354	0.0359	0.0325	0.0334	0.0385	0.0441
0.0176	0.0371	0.0367	0.0339	0.0349	0.0387	0.0457
0.0201	0.0385	0.0394	0.0355	0.0365	0.0401	0.0471
0.0226	0.0399	0.0398	0.0367	0.0387	0.0393	0.0471

[2]Only spatially averaged values of stresses were listed in the table. $\langle U \rangle_* = 0.0055 m/s$ was used for this case.

0.0251	0.0408	0.0401	0.0392	0.0390	0.0402	0.0472
0.0301	0.0407	0.0397	0.0401	0.0394	0.0399	0.0493
0.0351	0.0420	0.0397	0.0402	0.0384	0.0392	0.0477
0.0401	0.0398	0.0386	0.0392	0.0391	0.0383	0.0480
0.0451	0.0416	0.0414	0.0390	0.0380	0.0388	0.0477
0.0501	0.0415	0.0413	0.0394	0.0385	0.0388	0.0474
0.0551	0.0413	0.0419	0.0391	0.0392	0.0389	0.0477
0.0601	0.0415	0.0419	0.0404	0.0406	0.0382	0.0456
0.0651	0.0414	0.0417	0.0416	0.0404	0.0383	0.0467
0.0701	0.0409	0.0429	0.0418	0.0410	0.0407	0.0451
0.0801	0.0386	0.0427	0.0444	0.0470	0.0488	0.0484

$z\ (m)$	$\overline{u}\ (m/s)$ at $y/ds = 0.4$	$\overline{u}\ (m/s)$ at $y/ds = 0.53$	$\overline{u}\ (m/s)$ at $y/ds = 0.67$	$\overline{u}\ (m/s)$) at $y/ds = 0.8$	$\overline{u}\ (m/s)$ at $y/ds = 1$	$\langle\overline{u}\rangle\ (m/s)$ Spatial average
0.0001	0.0027	0.0070	0.0078	0.0080	0.0062	0.0043
0.0003	0.0055	0.0116	0.0141	0.0135	0.0123	0.0089
0.0005	0.0106	0.0197	0.0192	0.0175	0.0177	0.0140
0.0007	0.0187	0.0265	0.0257	0.0256	0.0211	0.0201
0.0009	0.0232	0.0296	0.0311	0.0279	0.0289	0.0243
0.0011	0.0279	0.0338	0.0342	0.0311	0.0331	0.0281
0.0016	0.0362	0.0418	0.0431	0.0407	0.0423	0.0364
0.0021	0.0453	0.0484	0.0483	0.0452	0.0484	0.0424
0.0031	0.0547	0.0551	0.0532	0.0524	0.0541	0.0500
0.0041	0.0593	0.0589	0.0570	0.0554	0.0575	0.0543
0.0051	0.0616	0.0608	0.0581	0.0565	0.0590	0.0558
0.0061	0.0620	0.0623	0.0589	0.0580	0.0598	0.0564
0.0071	0.0612	0.0623	0.0594	0.0579	0.0595	0.0557
0.0081	0.0600	0.0616	0.0596	0.0581	0.0604	0.0549
0.0091	0.0576	0.0603	0.0582	0.0582	0.0601	0.0536
0.0101	0.0550	0.0597	0.0584	0.0578	0.0595	0.0522
0.0126	0.0517	0.0570	0.0578	0.0579	0.0604	0.0503
0.0151	0.0518	0.0558	0.0569	0.0570	0.0592	0.0500
0.0176	0.0519	0.0558	0.0567	0.0566	0.0580	0.0502
0.0201	0.0530	0.0559	0.0574	0.0567	0.0583	0.0510
0.0226	0.0541	0.0573	0.0571	0.0560	0.0588	0.0514
0.0251	0.0528	0.0571	0.0570	0.0568	0.0595	0.0517
0.0301	0.0552	0.0574	0.0584	0.0578	0.0607	0.0527

0.0351	0.0547	0.0582	0.0587	0.0584	0.0616	0.0527
0.0401	0.0551	0.0581	0.0583	0.0580	0.0618	0.0526
0.0451	0.0548	0.0581	0.0581	0.0577	0.0626	0.0526
0.0501	0.0543	0.0582	0.0586	0.0582	0.0627	0.0527
0.0551	0.0546	0.0574	0.0592	0.0587	0.0635	0.0530
0.0601	0.0538	0.0570	0.0582	0.0582	0.0629	0.0524
0.0651	0.0523	0.0580	0.0593	0.0598	0.0644	0.0531
0.0701	0.0523	0.0584	0.0593	0.0596	0.0635	0.0531
0.0801	0.0558	0.0592	0.0594	0.0596	0.0644	0.0551

Table A.4: Experimental data for Fig.4-5, corresponding to case 3.1.

y/ds	$H_v(y)$ (m)	$U_*(y)$ (m/s)
0.00	0.0054	0.0039
0.03	0.0054	0.0039
0.07	0.0043	0.0043
0.13	0.0037	0.0046
0.20	0.0035	0.0048
0.27	0.0043	0.0047
0.40	0.0040	0.0052
0.53	0.0036	0.0057
0.67	0.0035	0.0058
0.80	0.0037	0.0056
1.00	0.0041	0.0055

3

[3]For case 3.1, the friction velocity fitted from the spatially averaged velocity $\langle U \rangle_* = 0.0055m/s$, and the fitted height of the linear stress layer $H_{vo} = 0.0035m$.The spatial average of local friction velocity $\langle U_* \rangle = 0.0052m/s$.

Table A.5: Fitted $\langle U \rangle_*$ and H_{vo} used in Fig.4-6,4-7,4-8 and 4-8. Case 4.4 has been excluded from our analysis because significant surface waves were observed in this case.

	$\langle U \rangle_* \ (m/s)$	$H_{vo} \ (m)$
Bare Channel		
Case 1.1	0.0030 +/- 0.0001	0.0083 +/- 0.0023
Case 1.2	0.0060 +/- 0.0005	0.0032 +/- 0.0009
Case 1.3	0.0024 +/- 0.0003	0.0096 +/- 0.0027
Case 1.4	0.0056 +/- 0.0004	0.0036 +/- 0.0010
Emergent vegetation		
Case 2.1	0.0016 +/- 0.0001	0.0110 +/- 0.0020
Case 2.2	0.0058 +/- 0.0007	0.0056 +/- 0.0015
Case 2.3	0.0040 +/- 0.0003	0.0065 +/- 0.0010
Case 2.4	0.0039 +/- 0.0003	0.0064 +/- 0.0010
Case 3.1	0.0055 +/- 0.0003	0.0035 +/- 0.0005
Case 3.2	0.0088 +/- 0.0004	0.0023 +/- 0.0002
Case 3.3	0.0030 +/- 0.0002	0.0037 +/- 0.0006
Case 3.4	0.0051 +/- 0.0003	0.0028 +/- 0.0003
Case 4.1	0.0059 +/- 0.0010	0.0032 +/- 0.0013
Case 4.2	0.0024 +/- 0.0006	0.0034 +/- 0.0020
Case 4.3	0.0091 +/- 0.0013	0.0019 +/- 0.0005
Case 5.1	0.0041 +/- 0.0007	0.0056 +/- 0.0020
Case 5.2	0.0076 +/- 0.0013	0.0035 +/- 0.0013
Case 5.3	0.0042 +/- 0.0007	0.0048 +/- 0.0020
Case 5.4	0.0006 +/- 0.0001	0.0100 +/- 0.0080
Case 6.1	0.0130 +/- 0.0020	0.0017 +/- 0.0005
Case 6.2	0.0078 +/- 0.0007	0.0034 +/- 0.0008
Case 6.3	0.0031 +/- 0.0006	0.0035 +/- 0.0020
Case 6.4	0.0110 +/- 0.0020	0.0030 +/- 0.0008

Bibliography

[1] Bruce Abernethy and Ian D Rutherfurd. Where along a river's length will vegetation most effectively stabilise stream banks. *Geomorphology*, 23(1):55–75, 1998.

[2] Steven R Abt, Warren P Clary, and Christopher I Thornton. Sediment deposition and entrapment in vegetated streambeds. *Journal of Irrigation and Drainage Engineering*, 120(6):1098–1111, 1994.

[3] Environmental Protection Agency. *The Quality of Our Nations Waters. A Summary of the National Water Quality Inventory: 1998 Report to Congress.* Office of Water, Washington DC. 841-S-00-001, 2000.

[4] Environmental Protection Agency. *National Rivers and Streams Assessment.* Office of Wetlands, Oceans and Watersheds Office of Research and Development,Washington, DC. EPA/841/D-13/001, 2008-2009.

[5] Millennium Ecosystem Assessment et al. *Ecosystems and human well-being*, volume 5. Island Press Washington, DC, 2005.

[6] CE Beeson and PF Doyle. Comparison of bank erosion at vegetated and non-vegetated channel bends1. *JAWRA Journal of the American Water Resources Association*, 31(6):983–990, 1995.

[7] Sean J Bennett, Weiming Wu, Carlos V Alonso, and Sam SY Wang. Modeling fluvial response to in-stream woody vegetation: implications for stream corridor restoration. *Earth Surface Processes and Landforms*, 33(6):890–909, 2008.

[8] Walter Berry, Norman Rubinstein, Brian Melzian, and Brian Hill. The biological effects of suspended and bedded sediment (sabs) in aquatic systems: a review. *United States Environmental Protection Agency, Duluth*, 2003.

[9] Pascale M Biron, Colleen Robson, Michel F Lapointe, and Susan J Gaskin. Comparing different methods of bed shear stress estimates in simple and complex flow fields. *Earth Surface Processes and Landforms*, 29(11):1403–1415, 2004.

[10] Philip J Blackmar, Daniel T Cox, and Wei-Cheng Wu. Laboratory observations and numerical simulations of wave height attenuation in heterogeneous vegetation. *Journal of Waterway, Port, Coastal, and Ocean Engineering*, 140(1):56–65, 2013.

[11] TJ Bouma, LA Van Duren, S Temmerman, T Claverie, A Blanco-Garcia, T Ysebaert, and PMJ Herman. Spatial flow and sedimentation patterns within patches of epibenthic structures: Combining field, flume and modelling experiments. *Continental Shelf Research*, 27(8):1020–1045, 2007.

[12] Mark M Brinson. *Riparian ecosystems: their ecology and status.* Eastern Energy Land Use Team [and] National Water Resources Analysis Group, US Fish and Wildlife Service, 1981.

[13] W. James Catallo. Ecotoxicology and wetland ecosystems: Current understanding and future needs. *Environmental Toxicology and Chemistry*, 12(12):2209–2224, 1993.

[14] A Cattaneo and J Kalff. The relative contribution of aquatic macrophytes and their epiphytes to the production of macrophyte beds1. *Limnology and Oceanography*, 25(2):280–289, 1980.

[15] PA Chambers and EE Prepas. Nutrient dynamics in riverbeds: the impact of sewage effluent and aquatic macrophytes. *Water Research*, 28(2):453–464, 1994.

[16] PA Chambers, EE Prepas, ML Bothwell, and HR Hamilton. Roots versus shoots in nutrient uptake by aquatic macrophytes in flowing waters. *Canadian Journal of Fisheries and Aquatic Sciences*, 46(3):435–439, 1989.

[17] PA Chambers, EE Prepas, HR Hamilton, and ML Bothwell. Current velocity and its effect on aquatic macrophytes in flowing waters. *Ecological Applications*, pages 249–257, 1991.

[18] Robert Costanza, Ralph d'Arge, Rudolf de Groot, Stephen Farber, Monica Grasso, Bruce Hannon, Karin Limburg, Shahid Naeem, Robert V O'Neill, Jose Paruelo, et al. The value of the world's ecosystem services and natural capital. 1998.

[19] DW Crowder and P Diplas. Using two-dimensional hydrodynamic models at scales of ecological importance. *Journal of hydrology*, 230(3):172–191, 2000.

[20] Finn Danielsen, Mikael K Sørensen, Mette F Olwig, Vaithilingam Selvam, Faizal Parish, Neil D Burgess, Tetsuya Hiraishi, Vagarappa M Karunagaran, Michael S Rasmussen, Lars B Hansen, et al. The asian tsunami: a protective role for coastal vegetation. *Science(Washington)*, 310(5748):643, 2005.

[21] John W Day Jr, Francesco Scarton, Andrea Rismondo, and Daniele Are. Rapid deterioration of a salt marsh in venice lagoon, italy. *Journal of Coastal Research*, pages 583–590, 1998.

[22] Linda A Deegan, David Samuel Johnson, R Scott Warren, Bruce J Peterson, John W Fleeger, Sergio Fagherazzi, and Wilfred M Wollheim. Coastal eutrophication as a driver of salt marsh loss. *Nature*, 490(7420):388–392, 2012.

[23] PATRICK DENNY. Solute movement in submerged angiosperms. *Biological Reviews*, 55(1):65–92, 1980.

[24] AH Elliott. Settling of fine sediment in a channel with emergent vegetation. *Journal of Hydraulic Engineering*, 126(8):570–577, 2000.

[25] VPE Evrard, Wawan Kiswara, Tjeerd J Bouma, and Jack J Middelburg. Nutrient dynamics of seagrass ecosystems: 15n evidence for the importance of particulate organic matter and root systems. *Marine Ecology Progress Series*, 295, 2005.

[26] Sergio Fagherazzi, Matthew L Kirwan, Simon M Mudd, Glenn R Guntenspergen, Stijn Temmerman, Andrea D'Alpaos, Johan Koppel, John M Rybczyk, Enrique Reyes, Chris Craft, et al. Numerical models of salt marsh evolution: Ecological, geomorphic, and climatic factors. *Reviews of Geophysics*, 50(1), 2012.

[27] Sergio Fagherazzi, Giuilio Mariotti, Patricia Wiberg, and Karen McGlathery. Marsh collapse does not require sea level rise. 2013.

[28] Food FAO et al. State of the world's forests-2003. 2003.

[29] John Finnigan. Turbulence in plant canopies. *Annual Review of Fluid Mechanics*, 32(1):519–571, 2000.

[30] Esperança Gacia and Carlos M Duarte. Sediment retention by a mediterranean posidonia oceanica meadow: the balance between deposition and resuspension. *Estuarine, coastal and shelf science*, 52(4):505–514, 2001.

[31] Walter Hans Graf. *Hydraulics of sediment transport.* Water Resources Publication, 1984.

[32] Watson W Gregg and Fred L Rose. The effects of aquatic macrophytes on the stream microenvironment. *Aquatic botany*, 14:309–324, 1982.

[33] Lucie Guo. Doing battle with the green monster of taihu lake. *Science*, 317(5842):1166–1166, 2007.

[34] Gwendolyn Gyssels and Jean Poesen. The importance of plant root characteristics in controlling concentrated flow erosion rates. *Earth Surface Processes and Landforms*, 28(4):371–384, 2003.

[35] Gwendolyn Gyssels, Jean Poesen, E Bochet, and Yong Li. Impact of plant roots on the resistance of soils to erosion by water: a review. *Progress in Physical Geography*, 29(2):189–217, 2005.

[36] Donald A Hammer. *Constructed wetlands for wastewater treatment: municipal, industrial and agricultural.* CRC Press, 1989.

[37] JI Hansen and F Ostergaard Andersen. Effects of phragmites australis roots and rhizomes on redox potentials, nitrification and bacterial numbers in the sediment. In *Proceedings of the 9th Nordic Symposium on Sediments*, pages 72–88. Scripta Limnologica Norr Malmo, Sweden, 1981.

[38] Jennifer J Harrod. The distribution of invertebrates on submerged aquatic plants in a chalk stream. *The Journal of Animal Ecology*, pages 335–348, 1964.

[39] JW Hayes and IG Jowett. Microhabitat models of large drift-feeding brown trout in three new zealand rivers. *North American journal of fisheries management*, 14(4):710–725, 1994.

[40] Tang Hongwu, H Wang, DF Liang, SQ Lv, and L Yan. Incipient motion of sediment in the presence of emergent rigid vegetation. *Journal of Hydro-environment Research*, 7(3):202–208, 2013.

[41] Ming Hua, Shujuan Zhang, Bingcai Pan, Weiming Zhang, Lu Lv, and Quanxing Zhang. Heavy metal removal from water/wastewater by nanosized metal oxides: a review. *Journal of Hazardous Materials*, 211:317–331, 2012.

[42] EB Jones, Gene S Helfman, Joshua O Harper, and Paul V Bolstad. Effects of riparian forest removal on fish assemblages in southern appalachian streams. *Conservation Biology*, 13(6):1454–1465, 1999.

[43] Angelina A Jordanova and CS James. Experimental study of bed load transport through emergent vegetation. *Journal of Hydraulic Engineering*, 129(6):474–478, 2003.

[44] Lynda Knobeloch, Barbara Salna, Adam Hogan, Jeffrey Postle, and Henry Anderson. Blue babies and nitrate-contaminated well water. *Environmental Health Perspectives*, 108(7):675, 2000.

[45] Umesh C Kothyari, Haruyuki Hashimoto, and Kenjirou Hayashi. Effect of tall vegetation on sediment transport by channel flows. *Journal of Hydraulic Research*, 47(6):700–710, 2009.

[46] PK Kundu and IM Cohen. *Fluid Mechanics. 2004.* Elsevier Academic Press, 2008.

[47] John Kuo. Morphology, anatomy and histochemistry of the australian seagrasses of the genus posidonia könig (posidoniaceae). i. leaf blade and leaf sheath of posidonia australis hook f. *Aquatic Botany*, 5:171–190, 1978.

[48] Lynn A Leonard, Albert C Hine, and Mark E Luther. Surficial sediment transport and deposition processes in a juncus roemerianus marsh, west-central florida. *Journal of Coastal Research*, pages 322–336, 1995.

[49] Anne F Lightbody and Heidi M Nepf. Prediction of velocity profiles and longitudinal dispersion in salt marsh vegetation. *Limnology and Oceanography*, 51(1):218–228, 2006.

[50] D Liu, P Diplas, JD Fairbanks, and CC Hodges. An experimental study of flow through rigid vegetation. *Journal of Geophysical Research: Earth Surface (2003–2012)*, 113(F4), 2008.

[51] Fabián López and Marcelo H García. Mean flow and turbulence structure of open-channel flow through non-emergent vegetation. *Journal of Hydraulic Engineering*, 127(5):392–402, 2001.

[52] Mitul Luhar, Jeffrey Rominger, and Heidi Nepf. Interaction between flow, transport and vegetation spatial structure. *Environmental Fluid Mechanics*, 8(5-6):423–439, 2008.

[53] M Marani, A d'Alpaos, S Lanzoni, and M Santalucia. Understanding and predicting wave erosion of marsh edges. *Geophysical Research Letters*, 38(21), 2011.

[54] Ross Mars, Kuruvilla Mathew, and Goen Ho. The role of the submergent macrophyte triglochin huegelii in domestic greywater treatment. *Ecological Engineering*, 12(1):57–66, 1999.

[55] SR Massel, K Furukawa, and RM Brinkman. Surface wave propagation in mangrove forests. *Fluid Dynamics Research*, 24(4):219–249, 1999.

[56] Maeve McBride, W Cully Hession, Donna M Rizzo, and Douglas M Thompson. The influence of riparian vegetation on near-bank turbulence: A flume experiment. *Earth Surface Processes and Landforms*, 32(13):2019–2037, 2007.

[57] Young John McGaha. The limnological relations of insects to certain aquatic flowering plants. *Transactions of the American Microscopical Society*, pages 355–381, 1952.

[58] ER Micheli and JW Kirchner. Effects of wet meadow riparian vegetation on streambank erosion. 2. measurements of vegetated bank strength and consequences for failure mechanics. *Earth Surface Processes and Landforms*, 27(7):687–697, 2002.

[59] William J Mitsch and Sven Erik Jørgensen. *Ecological engineering and ecosystem restoration.* John Wiley & Sons, 2004.

[60] Christian Nellemann and Emily Corcoran. *Blue carbon: the role of healthy oceans in binding carbon: a rapid response assessment.* UNEP/Earthprint, 2009.

[61] Heidi M Nepf. Flow and transport in regions with aquatic vegetation. *Annual review of fluid mechanics*, 44:123–142, 2012.

[62] Heidi M Nepf. Hydrodynamics of vegetated channels. *Journal of Hydraulic Research*, 50(3):262–279, 2012.

[63] HM Nepf. Drag, turbulence, and diffusion in flow through emergent vegetation. *Water resources research*, 35(2):479–489, 1999.

[64] HM Nepf and ER Vivoni. Flow structure in depth-limited, vegetated flow. *Journal of Geophysical Research: Oceans (1978–2012)*, 105(C12):28547–28557, 2000.

[65] Iehisa Nezu. *Turbulence in open-channel flows*. 1993.

[66] Iehisa Nezu and Wolfgang Rodi. Open-channel flow measurements with a laser doppler anemometer. *Journal of Hydraulic Engineering*, 112(5):335–355, 1986.

[67] Vladimir Nikora, Katinka Koll, Ian McEwan, Stephen McLean, and Andreas Dittrich. Velocity distribution in the roughness layer of rough-bed flows. *Journal of Hydraulic Engineering*, 130(10):1036–1042, 2004.

[68] Vladimir Nikora, Ian McEwan, Stephen McLean, Stephen Coleman, Dubravka Pokrajac, and Roy Walters. Double-averaging concept for rough-bed open-channel and overland flows: Theoretical background. *Journal of Hydraulic Engineering*, 133(8):873–883, 2007.

[69] State Environmental Protection Administration of China. *2013 Report on the State of China's Environment (in Chinese)*. 2013.

[70] US Commission on Ocean Policy. An ocean blueprint for the 21st century, 2004.

[71] Muhammad Akhir Othman. Value of mangroves in coastal protection. In *Ecology and Conservation of Southeast Asian Marine and Freshwater Environments including Wetlands*, pages 277–282. Springer, 1994.

[72] PM Outridge and BN Noller. Accumulation of toxic trace elements by freshwater vascular plants. In *Reviews of Environmental Contamination and Toxicology*, pages 1–63. Springer, 1991.

[73] Morten Pejrup, Jens Valeur, and Anders Jensen. Vertical fluxes of particulate matter in aarhus bight, denmark. *Continental Shelf Research*, 16(8):1047–1064, 1996.

[74] Linwood Pendleton, Daniel C Donato, Brian C Murray, Stephen Crooks, W Aaron Jenkins, Samantha Sifleet, Christopher Craft, James W Fourqurean, J Boone Kauffman, Núria Marbà, et al. Estimating global blue carbon emissions from conversion and degradation of vegetated coastal ecosystems. *PLoS One*, 7(9):e43542, 2012.

[75] Natasha Pollen and Andrew Simon. Estimating the mechanical effects of riparian vegetation on stream bank stability using a fiber bundle model. *Water Resources Research*, 41(7), 2005.

[76] Ian P Prosser, William E Dietrich, and Janelle Stevenson. Flow resistance and sediment transport by concentrated overland flow in a grassland valley. *Geomorphology*, 13(1):71–86, 1995.

[77] Larry J Puckett. Identifying the major sources of nutrient water pollution. *Environmental Science & Technology*, 29(9):408A–414A, 1995.

[78] Jane Qiu. China to spend billions cleaning up groundwater. *Science*, 334(6057):745–745, 2011.

[79] MR Raupach and RH Shaw. Averaging procedures for flow within vegetation canopies. *Boundary-Layer Meteorology*, 22(1):79–90, 1982.

[80] Jeffrey T Rominger, Anne F Lightbody, and Heidi M Nepf. Effects of added vegetation on sand bar stability and stream hydrodynamics. *Journal of Hydraulic Engineering*, 136(12):994–1002, 2010.

[81] Jeremy David Rouse, Christine A Bishop, and John Struger. Nitrogen pollution: an assessment of its threat to amphibian survival. *Environmental health perspectives*, 107(10):799, 1999.

[82] PAWEŁ M ROWIŃSKI and Janusz Kubrak. A mixing-length model for predicting vertical velocity distribution in flows through emergent vegetation. *Hydrological sciences journal*, 47(6):893–904, 2002.

[83] P. G. Salvador, T. Stoesser, A.C. Rummel, and W Rodi. Turbulent flow structures of shallow flows through vegetation. *IProc. IAHR Fifth International Symposium on Environmental Hydraulics (ISEH V), Arizona, USA*, 2007.

[84] Kaj Sand-jensen. Influence of submerged macrophytes on sediment composition and near-bed flow in lowland streams. *Freshwater Biology*, 39(4):663–679, 1998.

[85] KAJ SAND-JENSEN and TOM VindbÆK Madsen. Patch dynamics of the stream macrophyte, callitriche cophocarpa. *Freshwater Biology*, 27(2):277–282, 1992.

[86] KAJ SAND-JLNSEN, ERIK JEPPESEN, KURT NIELSEN, LILLIAN BIJL, LUISE HJERMIND, LISBETH WIGGERS NIELSEN, and TORBEN MOTH IVLRSLN. Growth of macrophytes and ecosystem consequences in a lowland danish stream. *Freshwater Biology*, 22(1):15–32, 1989.

[87] Hans-Henrik Schierup and Vagn Juhl Larsen. Macrophyte cycling of zinc, copper, lead and cadmium in the littoral zone of a polluted and a non-polluted lake. i. availability, uptake and translocation of heavy metals in phragmites australis (cav.) trin. *Aquatic Botany*, 11:197–210, 1981.

[88] Marcus Schulz, Hans-Peter Kozerski, Thomas Pluntke, and Karina Rinke. The influence of macrophytes on sedimentation and nutrient retention in the lower river spree (germany). *Water Research*, 37(3):569–578, 2003.

[89] FD Shields, AJ Bowie, and CM Cooper. Control of streambank erosion due to bed degradation with vegetation and structure1. *JAWRA Journal of the American Water Resources Association*, 31(3):475–489, 1995.

[90] Andrew Simon and Andrew JC Collison. Quantifying the mechanical and hydrologic effects of riparian vegetation on streambank stability. *Earth Surface Processes and Landforms*, 27(5):527–546, 2002.

[91] Anita Singh, Rajesh Kumar Sharma, Madhoolika Agrawal, and Fiona M Marshall. Health risk assessment of heavy metals via dietary intake of foodstuffs from the wastewater irrigated site of a dry tropical area of india. *Food and Chemical Toxicology*, 48(2):611–619, 2010.

[92] KR Stapleton and DA Huntley. Seabed stress determinations using the inertial dissipation method and the turbulent kinetic energy method. *Earth Surface Processes and Landforms*, 20(9):807–815, 1995.

[93] T Stoesser, SJ Kim, and P Diplas. Turbulent flow through idealized emergent vegetation. *Journal of Hydraulic Engineering*, 136(12):1003–1017, 2010.

[94] Ross A Sutherland. Lead in grain size fractions of road-deposited sediment. *Environmental Pollution*, 121(2):229–237, 2003.

[95] Bernard W Sweeney, Thomas L Bott, John K Jackson, Louis A Kaplan, J Denis Newbold, Laurel J Standley, W Cully Hession, and Richard J Horwitz. Riparian deforestation, stream narrowing, and loss of stream ecosystem services. *Proceedings of the National Academy of Sciences of the United States of America*, 101(39):14132–14137, 2004.

[96] Rudy SWENNEN, Huu Hieu HO, and An Van Damme. Distribution and contamination status of heavy metals in estuarine sediments near cua ong harbor, ha long bay, vietnam. *Geologica Belgica*, 2009.

[97] Michal Tal and Chris Paola. Dynamic single-thread channels maintained by the interaction of flow and vegetation. *Geology*, 35(4):347–350, 2007.

[98] Norio Tanaka. Vegetation bioshields for tsunami mitigation: review of effectiveness, limitations, construction, and sustainable management. *Landscape and Ecological Engineering*, 5(1):71–79, 2009.

[99] Yukie Tanino and Heidi M Nepf. Laboratory investigation of mean drag in a random array of rigid, emergent cylinders. *Journal of Hydraulic Engineering*, 134(1):34–41, 2008.

[100] Chris C Tanner, John S Clayton, and Martin P Upsdell. Effect of loading rate and planting on treatment of dairy farm wastewaters in constructed wetlandsii. removal of nitrogen and phosphorus. *Water research*, 29(1):27–34, 1995.

[101] George Tchobanoglous and Franklin L Burton. Wastewater engineering. *Management*, 7:1–4, 1991.

[102] S Temmerman, TJ Bouma, J Van de Koppel, D Van der Wal, MB De Vries, and PMJ Herman. Vegetation causes channel erosion in a tidal landscape. *Geology*, 35(7):631–634, 2007.

[103] U Türker, O Yagci, and MS Kabdaşlı. Analysis of coastal damage of a beach profile under the protection of emergent vegetation. *Ocean Engineering*, 33(5):810–828, 2006.

[104] Ivan Valiela and Marci L Cole. Comparative evidence that salt marshes and mangroves may protect seagrass meadows from land-derived nitrogen loads. *Ecosystems*, 5(1):92–102, 2002.

[105] DE Walling, PN Owens, J Carter, GJL Leeks, Scott Lewis, AA Meharg, and J Wright. Storage of sediment-associated nutrients and contaminants in river channel and floodplain systems. *Applied Geochemistry*, 18(2):195–220, 2003.

[106] Luke L Warren, Roger S Wotton, Geraldene Wharton, Jonathon AB Bass, and Jacqueline A Cotton. The transport of fine particulate organic matter in vegetated chalk streams. *Ecohydrology*, 2(4):480–491, 2009.

[107] Peter R Wilcock. Estimating local bed shear stress from velocity observations. *Water Resources Research*, 32(11):3361–3366, 1996.

[108] Douglas P Wilson. The decline of zostera marina l. at salcombe and its effects on the shore. *Journal of the Marine Biological Association of the United Kingdom*, 28(02):395–412, 1949.

[109] L Windham, JS Weis, and P Weis. Uptake and distribution of metals in two dominant salt marsh macrophytes, spartina alterniflora (cordgrass) and phragmites australis (common reed). *Estuarine, Coastal and Shelf Science*, 56(1):63–72, 2003.

[110] EM Yager and MW Schmeeckle. The influence of vegetation on turbulence and bed load transport. *Journal of Geophysical Research: Earth Surface*, 118(3):1585–1601, 2013.

[111] M Selim Yalin. *Mechanics of sediment transport.* Pergamon press, 2013.

[112] Hongtao Zhao, Xuyong Li, Xiaomei Wang, and Di Tian. Grain size distribution of road-deposited sediment and its contribution to heavy metal pollution in urban runoff in beijing, china. *Journal of hazardous materials*, 183(1):203–210, 2010.